Tropical Cyclone Potential Size

DANYANG WANG,[a,b] YANLUAN LIN,[a] AND DANIEL R. CHAVAS[b]

[a] *Ministry of Education Key Laboratory for Earth System Modeling, Department of Earth System Science, Tsinghua University, Beijing, China*
[b] *Purdue University, West Lafayette, Indiana*

(Manuscript received 14 December 2021, in final form 6 June 2022)

ABSTRACT: A model for tropical cyclone (TC) potential size (PS), which is capable of predicting the equilibrium outer radius of a TC solely from environmental parameters, is proposed. The model combines an updated Carnot cycle model with a physical model for the wind profile, which serve as energetic and dynamic constraints, respectively, on the minimum pressure. Physically, the Carnot cycle model defines how much the surface pressure can be dropped energetically, and the wind profile model defines how large the steady-state storm needs to be to yield that pressure drop for a given maximum wind speed. The model yields an intrinsic length scale V_{Carnot}/f, with f the Coriolis parameter, V_{Carnot} similar to the potential intensity V_p, but without a dependence on the surface exchange coefficients of enthalpy C_k and momentum C_d. Analytic tests with the theory varying outflow temperature, sea surface temperature (SST), and f demonstrate that the model predictions are qualitatively consistent with the V_p/f scaling for outer size found in past work. The model also predicts a weak dependence of outer size on C_d, C_k, and horizontal mixing length l_h of turbulence, consistent with numerical simulation results. Idealized numerical simulation experiments with varied tropopause temperature, SST, f, C_d, C_k, and l_h show that the model performs well in predicting the simulated outer radius. The V_{Carnot}/f scaling also better captures the dependence of simulated TC size on SST than V_p/f. Overall, the model appears to capture the essential physics that determine equilibrium TC size on the f plane.

KEYWORDS: Hurricanes/typhoons; Thermodynamics; Energy budget/balance

1. Introduction

Theoretical models have produced analytical solutions for the upper bound of tropical cyclone (TC) intensity, known as potential intensity (PI; V_p), solely from environmental parameters (Emanuel 1986, 1988; Emanuel and Rotunno 2011, hereafter ER11; Rousseau-Rizzi and Emanuel 2019). PI theory, derived from several assumptions, such as the assumption of slantwise neutrality of the eyewall structure, generally states that the PI of a TC is influenced by air–sea enthalpy disequilibrium, temperature difference of surface and tropopause air, and sea surface exchange coefficients of enthalpy C_k and momentum C_d. However, there does not currently exist a theory to predict the overall size of a TC, defined as the outer radius where near-surface winds vanish (r_a), solely from environmental parameters. In fact, r_a is an input parameter in several physical models of TC wind structure (ER11; Chavas et al. 2015, hereafter C15).

Idealized numerical simulations in previous studies indicate that the quasi-equilibrium state of a TC on the f plane can be maintained for tens of days or longer (Khairoutdinov and Emanuel 2013; Zhou et al. 2014; Chavas and Emanuel 2014, hereafter CE14; Cronin and Chavas 2019; Rousseau-Rizzi et al. 2021). CE14 showed that V_p/f, with f the Coriolis parameter, is a natural length scale for the equilibrium value of r_a for mature TCs on an f plane. A similar radial length scale $\sqrt{\chi}/f$, where $\sqrt{\chi}$ is similar to V_p but without the C_k/C_d factor (or simply taken to be 1), has also been proposed as the intrinsic TC length scale in the theory of Emanuel (1989, 1995). However, there lack explicit mechanistic explanations for why equilibrium TC size should scale with V_p/f. Khairoutdinov and Emanuel (2013) and Emanuel (2022) derived another scaling $\sqrt{L_v q_b}/f$ for equilibrium TC size with q_b the boundary layer specific humidity, based on energy and entropy budgets. In nature, though, median TC size appears to scale with the Rhines scale (Chavas et al. 2016; Chavas and Reed 2019; Lu and Chavas 2022), which depends on $\beta^{-1/2}$, as this scale is much smaller than the f^{-1} scale in Earth's tropics where f is relatively small and β is relatively large. However, there is observational evidence that the upper bound of TC size does indeed scale with V_p/f (Fig. 5c of Chavas et al. 2016), even if most storms are substantially smaller than this length scale likely owing to the effects of β.

In this study, we propose a model for the maximum potential TC size on an f plane defined solely from environmental parameters. The model yields an intrinsic scaling for equilibrium TC size and explains why equilibrium TC size appears to follow a V_p/f length scale on an f plane when C_k/C_d is held fixed as found in past work. The scaling is similar to V_p/f but without the C_k/C_d factor; hence, it is closely related to $\sqrt{\chi}/f$ and $\sqrt{L_v q_b}/f$. Since the C_k/C_d factor is nondimensional, dimensional analysis alone cannot determine whether this factor should or should not exist in V_p/f length scale, so the distinction between V_p/f and $\sqrt{\chi}/f$ is ambiguous. As C_k/C_d is often taken as approximately 1, their magnitudes will also be very similar. We test this theory, including the dependence on C_k and C_d, against idealized numerical simulations.

The basic idea of our model is as follows. It is known that steady-state TC size is constrained by the energetic cycle (i.e., Carnot cycle) of its air parcels, as is explicitly pointed out in

Corresponding author: Yanluan Lin, yanluan@tsinghua.edu.cn

DOI: 10.1175/JAS-D-21-0325.1

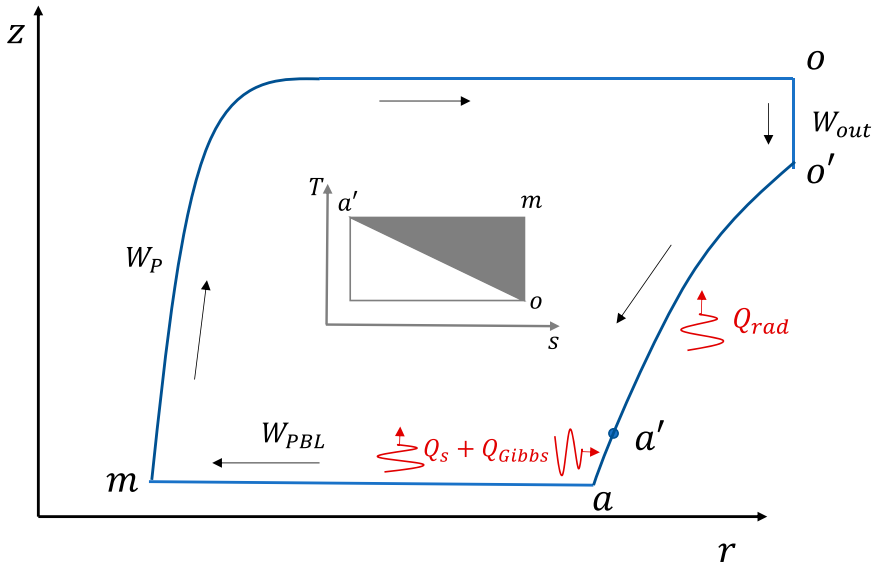

FIG. 1. Schematic path of a parcel in a updated Carnot cycle in a fully developed TC. Point a marks the radius of vanishing near surface wind and contains environmental relative humidity. Point m marks the radius of maximum wind. Point o marks the radially farthest point the parcel could reach in the outflow. Point o' has the same radius as o, but with a lower altitude. Point a' is spatially close to a where the parcel has near-zero relative humidity. The arrows mark the direction of the path and the path is a closed cycle. See text for different processes in the path. Inside the cycle is a schematic T–s diagram of the cycle.

Emanuel (1991): a larger size *decreases* the inner-core surface pressure deficit by requiring a larger work in the outflow to restore angular momentum lost to surface friction (though we will discuss in the end that this outflow work is not required to constrain TC size). On the other hand, through the TC wind profile (e.g., C15 model), TC size is constrained dynamically by the relationship between storm size and the surface pressure deficit via gradient wind balance (Chavas et al. 2017): given the same intensity, a larger size *increases* the inner-core surface pressure deficit. As the Carnot cycle model and C15 model are effectively independent of each other, a TC satisfying the two models may have a deterministic size. Thus, our hypothesis is that TC size (outer radius) can be determined by satisfying both energetic (Carnot cycle) and dynamical (C15 model) constraints simultaneously. Physically, the pressure drop experienced by inflowing parcels is limited by its energetic cycle, whereas the inner-core pressure deficit must increase as r_a increases via gradient wind balance; hence, there is a maximum potential size that satisfies both energetic and dynamical constraints.

The paper is organized as follows. In section 2, we introduce an updated Carnot cycle model and briefly review the C15 wind profile model. We then show how combining the updated Carnot cycle and C15 model predicts a unique equilibrium TC size. We show that this model can qualitatively reproduce the V_p/f scaling found in past work except for the dependence on C_k and C_d, and we propose a new length scale intrinsic to our model that can also capture this dependence on exchange coefficients. We refer to our approach as a model for TC potential size (PS) since it predicts a theoretical upper limit of TC outer radius and provides a new intrinsic length scale for this size. The TC outer size in this study is specifically the TC size at equilibrium state, and the word "equilibrium" will be omitted for brevity hereafter. In section 3, we test our TC PS model against idealized numerical simulations on an f plane by varying different environmental parameters. In section 4, we test whether our modifications to the Emanuel's Carnot cycle model are essential to the TC PS model predictions. In section 5, we summarize and discuss our findings.

2. Description of the model

a. An updated Carnot cycle model

As reviewed by Rousseau-Rizzi et al. (2021), the conceptual model of a closed thermodynamic cycle to describe a steady state TC was presented by Eliassen and Kleinschmidt (1957). The same concept was developed further by Emanuel (1986, 1988, 1991). Figure 1 shows a hypothetical path of an air parcel in an updated Carnot cycle in a fully developed TC. The updated Carnot cycle is qualitatively similar to the Emanuel's Carnot cycle (Emanuel 1986, 1988, 1991), but with three main modifications: 1) the parcel loses nearly all the water during the eyewall ascent and experiences a complete resaturation during the inflow leg rather than simply starting from a rather high relative humidity in the inflow without an explicit remoistening process; 2) radiative cooling is acting throughout both the outflow and descent legs rather than only acting in the upper troposphere at the outflow temperature; and 3) exchanges of Gibbs free energy of water species in the hydrological cycle are considered rather than neglected. The modifications are believed to

more realistically describe a hypothetical thermodynamic cycle of a TC, as it now includes an explicit treatment of the water budget and its energetics as part of the closed cycle, though the modifications are not critical to our final conclusions as shown in section 4. The complete resaturation tends to increase the net heat in the cycle but this effect is compensated by a longer path of radiative cooling and the inclusion of the exchanges of Gibbs free energies of water species.

We assume the parcel is able to complete a closed cycle, as it could in an idealized simulation (Hakim 2011; Rousseau-Rizzi et al. 2021), which does not have mass exchanges of dry air with the environment. Starting from the outer radius r_a near the surface (point a in Fig. 1), the parcel flows cyclonically inwards with constant temperature T_s, until reaching the radius of maximum wind r_m (point m in Fig. 1) where it begins to ascend. From point a to m, the parcel experiences boundary layer turbulent friction and loses most of its absolute angular momentum M. At the same time, via surface enthalpy fluxes, the parcel increases its entropy s from its environmental value at point a (s_a) to the highest value at point m (s_m). At point a, the relative humidity $\mathcal{H}$ of the parcel is equal to the environmental value $\mathcal{H}_e$; at point m, $\mathcal{H}$ is 1. From point m to o, the parcel experiences eyewall ascent to the tropopause and flows outwards to the farthest point o, where the parcel may achieve maximum anticyclonic velocity. The parcel loses nearly all of its water by precipitation in the eyewall. Note that M is conserved during this process and s is also nearly conserved during the eyewall ascent. From point o to o', the parcel descends below the upper-tropospheric anticyclone by restoring M to its original value at point a through turbulent mixing with the environment. From point o' to a, the parcel experiences inviscid descent conserving M. From o to a', the parcel subsides with no remoistening. From a' to a, the parcel is remoistened to ambient relative humidity. Hence, a' marks the top of boundary layer. For simplicity we do not distinguish the differences of temperature and dry air partial pressure between a' and a, as will be assumed below. During the outflow leg from m to o and the subsidence leg from o to a', radiative cooling plays the dominant role in gradually reducing the parcel entropy from s_m to its lowest value $s_{a'}$. This results in a triangular shape instead of a rectangle in the temperature–entropy (T–s) phase space of a thermodynamic cycle in a TC and, hence, an efficiency that is less than Carnot efficiency (Hakim 2011; Pauluis and Zhang 2017). The hydrological cycle is also associated with exchanges of Gibbs free energy (aka Gibbs potential), which is a Legendre transformed function of internal energy (Callen 1985), of water species. During the inflow, the parcel increases its water mass and imports low Gibbs free energy of water vapor; during the eyewall ascent, the parcel loses its water mass and exports relatively high Gibbs free energy of liquid water (Pauluis and Zhang 2017). Both processes decrease the available mechanical work done by the parcel in the cycle (Pauluis 2011; Pauluis and Zhang 2017).

We next formulate the updated Carnot cycle. The procedure is very similar to the original one in Emanuel (1991). Following an air parcel in a TC, the Bernoulli equation may be written as (see appendix A, following Romps 2008)

$$d\left[(1+q_t)\frac{1}{2}|\mathbf{V}|^2\right] = -\alpha_d\, dp + \mathbf{F}\cdot d\mathbf{l} + \phi\, dq_t - d[(1+q_t)\phi], \tag{1}$$

where $\mathbf{V}$ is three-dimensional velocity vector, q_t the total water mixing ratio, α_d the specific volume of dry air, p the pressure, $\mathbf{F}$ the frictional force per unit mass of dry air, $d\mathbf{l}$ a finite displacement of the parcel, and $\phi = \Gamma z$ the geopotential, with Γ the gravitational acceleration, and z the altitude. In Eq. (1) the diffusive fluxes of kinetic energy have been neglected.

The Gibbs relation may be written as

$$dh - \alpha_d\, dp = T\, ds + \sum g_w\, dq_w, \tag{2}$$

where h is the enthalpy of moist air per unit mass of dry air, T the temperature, s the moist entropy per unit mass of dry air, g_w the specific Gibbs free energy of water species, q_w the mixing ratio of water species, and subscript $w = v, l, s$ represents water vapor, liquid water, and solid water, respectively. Here entropy s is defined as

$$s \approx c_{pd}\ln\frac{T}{T_{\text{trip}}} - R\ln\frac{p_d}{p_0} + q_v\frac{L_v}{T} - q_v R_v \ln\mathcal{H}, \tag{3}$$

where c_{pd} is the specific heat of dry air at constant pressure, R the gas constant of dry air, R_v the gas constant of water vapor, L_v the latent heat of vaporization, $\mathcal{H}$ the relative humidity, p_d the partial pressure of dry air, T_{trip} and p_0 the triple-point temperature and a reference pressure, respectively. Ice phase has been neglected in this expression. The heat capacity of liquid water c_l and that of water vapor at constant pressure c_{pv} have also been neglected to be consistent with our treatment of Gibbs free energy below. This assumption also leads to a temperature independent L_v, taken as its value at the reference temperature.

Substituting Eq. (2) into Eq. (1) and integrating along a closed cycle gives

$$\oint T\, ds + \oint\sum g_w\, dq_w = -\oint\mathbf{F}\cdot d\mathbf{l} + \oint dW_p, \tag{4}$$

which states that heat added to the system is used to do mechanical work. Equation (4) is an updated version of the Emanuel Carnot cycle that now includes the exchanges of Gibbs free energy of water species $\oint\sum g_w\, dq_w$ and the work to lift water $W_p = \oint dW_p = \oint\Gamma q_t\, dz$ (Pauluis et al. 2000; Pauluis and Zhang 2017), which is transformed from the third term on the rhs of Eq. (1) (see also appendix A). Note that $\oint\sum g_w\, dq_w$ is typically negative (with properly chosen reference states of enthalpy and entropy) so that it reduces the mechanical work performed by the air parcel in a cycle (Pauluis and Zhang 2017). We may for simplicity symbolically define $Q_s = \oint T\, ds$ and $Q_{\text{Gibbs}} = \oint\sum g_w\, dq_w$. Following the Emanuel Carnot cycle model, frictional dissipation only occurs in the inflow and at large radii in the outflow. Thus, $-\oint\mathbf{F}\cdot d\mathbf{l} = W_{\text{PBL}} + W_{\text{out}}$ may be defined, with W_{PBL} and W_{out} denoting work against friction in the inflow and outflow, respectively. With the symbols defined above, Eq. (4) may be rewritten as

$$Q_s + Q_{\text{Gibbs}} = W_{\text{PBL}} + W_{\text{out}} + W_p. \tag{5}$$

We provide expressions for each term in Eq. (5) as follows. Q_s may be expanded:

$$\begin{aligned} Q_s &= \oint T\,ds = \eta\epsilon_C \int_{a'}^{m} T\,ds \approx \eta\epsilon_C T_s(s_m - s_{a'}) \\ &\approx \eta\epsilon_C\left(RT_s \ln\frac{p_{da}}{p_{dm}} + L_v q_{vm}\right), \end{aligned} \tag{6}$$

where $\epsilon_C = (T_s - T_o)/T_s$ is the Carnot efficiency, and η is a coefficient representing the efficiency relative to Carnot efficiency. For example, $\eta = 1/2$ for a triangle parcel trajectory in T–s phase space as noted above (e.g., Fig. 6a of Pauluis and Zhang 2017). Zero relative humidity has been assumed at point a'. The dry air partial pressure and temperature at a' have also been approximated as environmental values p_{da} and T_s, respectively; these errors are small as the second term in the bracket on the rhs of Eq. (6) is dominant.

As shown by Figs. 6d–f of Pauluis and Zhang (2017), $\oint \sum g_w\, dq_w$ (with the reference states chosen therein) is dominated by the import of negative Gibbs free energy of water vapor (g_v) in the near-surface inflow branch of the cycle, which may be written as

$$\begin{aligned} g_v &\approx R_v T \ln\mathcal{H} \\ &= R_v T \ln\frac{e}{e^*} \\ &\approx R_v T\left[\ln\left(\frac{R_v}{R}\, p_{da} q_v\right) - \ln e^*\right] \\ &= R_v T(\ln q_v + c_1), \end{aligned} \tag{7}$$

where the first line is defined on p. 94 of Pauluis (2011), e is the partial pressure of water vapor, e^* the saturation vapor pressure, and $c_1 = -\ln e^* + \ln[(R_v/R)p_{da}] = -\ln q^*_{va}$. The dry air partial pressure is set to p_{da}, and all remoistening is assumed to occur at this pressure to make the integration below tractable. We have used the relation that $q_v = (R/R_v)(e/p_d)$. Thus, with Eq. (7), $Q_{\text{Gibbs}} = \oint \sum g_w\, dq_w$ may be expanded:

$$\begin{aligned} Q_{\text{Gibbs}} &\approx \int_{a'-m} g_v dq_v \\ &= \int_{q_{va'}}^{q_{vm}} g_v dq_v \\ &= \int_{q_{va'}}^{q_{vm}} R_v T_s(\ln q_v + c_1) dq_v \\ &= R_v T_s \int_{q_{va'}}^{q_{vm}} \ln q_v\, dq_v + R_v T_s c_1 (q_{vm} - q_{va'}) \\ &\approx R_v T_s(-q_{vm} + q_{vm}\ln q_{vm}) + R_v T_s c_1 q_{vm} \\ &= -R_v T_s q_{vm} + R_v T_s q_{vm} \ln\frac{q_{vm}}{q^*_{va}} \\ &= -R_v T_s q_{vm} + R_v T_s q_{vm} \ln\frac{p_{da}}{p_{dm}}, \end{aligned} \tag{8}$$

where e^*_s is the near surface saturation vapor pressure and we have taken the limit of $q_{va'} \approx 0$ (i.e., air reentering the boundary layer has been almost fully dehydrated). This assumption follows that fact that tropical tropopause saturation water vapor mixing ratio should be on the order of 10^{-5} kg kg^{-1}. For the m–o leg, the exchange of Gibbs free energy is zero under assumption of $c_l \approx 0$. For the a'–a leg, from Eq. (8) we have $\int_{a'-a} g_v\, dq_v \approx -R_v T_s q_{va} + R_v T_s q_{va} \ln\mathcal{H}_a$, which constitutes the majority of Q_{Gibbs}.

Following the Emanuel Carnot cycle model (e.g., Emanuel 1991), work against friction $-\oint \mathbf{F}\cdot d\mathbf{l}$ is done principally at the surface during the inflow, where absolute angular momentum M is lost, and in the free atmosphere in the outflow where M is restored from the environment. M is defined by

$$M = rv + \frac{1}{2} fr^2, \tag{9}$$

where r is radius from the TC center, v the tangential velocity, and f the Coriolis parameter. By assuming hydrostatic balance in Eq. (1), assuming vanishing q_t, and using Eq. (9), the work done against friction in the outflow may be written:

$$\begin{aligned} W_{\text{out}} &= \int_o^{o'} -\mathbf{F}\cdot d\mathbf{l} \\ &= -\frac{1}{2}(v_{o'}^2 - v_o^2) \\ &= -\frac{1}{2}\left[\frac{M_{o'}^2 - M_o^2}{r_o^2} - f(M_{o'} - M_o) + \frac{1}{4}f^2(r_{o'}^2 - r_o^2)\right] \\ &= \frac{1}{2}\left[f(M_{o'} - M_o) - \frac{M_{o'}^2 - M_o^2}{r_o^2}\right] \\ &= \frac{1}{2}\left[f(M_a - M_m) - \frac{M_a^2 - M_m^2}{r_o^2}\right] \\ &= \frac{1}{4} f^2 r_a^2 - \frac{1}{2} fM_m - \frac{1}{2}\frac{M_a^2 - M_m^2}{r_o^2}, \end{aligned} \tag{10}$$

As there is no explicit theory for the size of the outflow r_o, we may for simplicity assume r_o to be infinitely large, which means M is restored in the environment at some large radius well beyond the storm, so that the last term in the last line of Eq. (10) can be ignored. Thus, we may have an approximation

$$W_{\text{out}} \approx \frac{1}{4} f^2 r_a^2 - \frac{1}{2} fM_m, \tag{11}$$

The approximation of Eq. (11) overestimates W_{out}. Making use of Eq. (1), the work done against friction in the inflow branch may be written:

$$\begin{aligned} W_{\text{PBL}} &= \int_a^m -\mathbf{F}\cdot d\mathbf{l} \\ &\approx \int_a^m -\alpha_d\, dp + \int_a^m -d\left[(1+q_t)\frac{1}{2}|\mathbf{V}|^2\right] \\ &\approx RT_s \ln\frac{p_{da}}{p_{dm}} - \frac{1}{2} V_{\max}^2, \end{aligned} \tag{12}$$

where the ideal gas law has been used assuming isothermal inflow at T_s and $V_{\max}$ is the maximum tangential wind of a TC near the top of boundary layer. The effect of water content on

$W_{\rm PBL}$ has been neglected. Note that a complete expression for $W_{\rm PBL}$ can be obtained by substitution of Eq. (2) again to eliminate $-\alpha_d dp$. This will yield two additional terms $R_v T_s q_{va} \ln\mathcal{H}_e + \int_a^m g_v dq_v$, on the order of -10^2 J kg^{-1}. As the moistening process is weak from a to m compared to that from a' to a, these terms are neglected for simplicity here. Additionally, $V_{\rm max}$ is typically located at the top of the boundary layer instead of near surface; the work against friction from surface to the location of $V_{\rm max}$ at r_m, would also be on the order of 10^2 J kg^{-1} assuming tangential frictional acceleration $\sim 10^{-2}$ m s^{-2}. The contribution of this as well as of the vertical change of total velocity, which both depend on detailed inner-core turbulence, is not considered here.

Finally, we parameterize W_p by taking

$$W_p = (\beta - 1)(W_{\rm PBL} + W_{\rm out}), \tag{13}$$

where β is a coefficient which may be taken as 5/4 by referring to Fig. 7a of Pauluis and Zhang (2017). This value means that the mechanical work to lift water is approximately 25% of the work against friction (or frictional dissipation) in the eyewall cycle. Note that this ratio would be much larger (~250%) for irrotational convection in tropics (e.g., Pauluis et al. 2000; Pauluis and Held 2002). A physical prediction for W_p in a cycle requires further study.

Substituting Eqs. (6), (8), (10), (12), and (13) into Eq. (5) gives

$$\begin{aligned}\eta\epsilon_C L_v q_{vm} - R_v T_s q_{vm} + R_v T_s q_{vm} \ln\frac{p_{da}}{p_{dm}} \\ = (\beta - \eta\epsilon_C) R T_s \ln\frac{p_{da}}{p_{dm}} + \beta\left(-\frac{1}{2} V_{\rm max}^2 + \frac{1}{4} f^2 r_a^2 \right. \\ \left. - \frac{1}{2} f M_m - \frac{1}{2}\frac{M_a^2 - M_m^2}{r_o^2}\right).\end{aligned} \tag{14}$$

By making use of $q_v = (R/R_v)(e/p_d)$ to relate q_v to p_d and defining

$$y = p_{da}/p_{dm}, \tag{15}$$

which is the ratio of the surface ambient dry air pressure to its value at the radius of maximum wind, we may write a succinct relation for y given by

$$y = \exp(Ay + By\ln y + C), \tag{16}$$

where

$$A = \frac{e_s^*}{p_{da}}\frac{\eta\epsilon_C L_v/R_v - T_s}{(\beta - \eta\epsilon_C)T_s}, \tag{17}$$

$$B = \frac{e_s^*}{p_{da}(\beta - \eta\epsilon_C)}, \tag{18}$$

$$C = -\frac{\beta\left(-\frac{1}{2} V_{\rm max}^2 + \frac{1}{4} f^2 r_a^2 - \frac{1}{2} f M_m - \frac{1}{2}\frac{M_a^2 - M_m^2}{r_o^2}\right)}{(\beta - \eta\epsilon_C) R T_s}. \tag{19}$$

Once p_{dm} is obtained from Eq. (16), p_m is obtained by $p_m = p_{dm} + e_s^*$. Taking the natural logarithm of Eq. (16) shows that the lhs is directly associated with $W_{\rm PBL}$ [via the $RT_s \ln(p_{da}/p_{dm})$ term in Eq. (12)], and thus, the rhs corresponds to the available work for frictional dissipation (net heating minus W_p) in the cycle minus frictional work in the outflow. $V_{\rm max}$ is taken to be either environmentally or externally defined. Equation (16) is directly analogous to Eq. (22) of Emanuel (1988). The roots of Eq. (16) are the intersections of the two curves represented by the lhs and rhs of Eq. (16), respectively. It can be shown that the second derivative of the rhs of Eq. (16) is always positive where $y > 0$. Thus, there may be one, two, or no roots for Eq. (16), similar to Emanuel (1988). In Eq. (16), A is completely determined by the thermodynamic environment corresponding to the net heating of the updated Carnot cycle. Increasing T_s or decreasing T_o individually or simultaneously would increase A (not shown). B arises from an approximation of taking p_{da} as the mean dry air partial pressure in the inflow leg for integration when calculating $Q_{\rm Gibbs}$ [Eqs. (7) and (8)]. Since B would be of the same order as A and $\ln y$ would be one order less than y if $y \lesssim 1.1$, then the $By\ln y$ term in Eq. (16) can be neglected. The primary effect from $Q_{\rm Gibbs}$ is the $-T_s$ term in A. Finally, C is primarily associated with work against friction in the outflow. C becomes negative for a sufficiently large TC.

We test whether Eq. (16) is able to produce reasonable pressure drops given some environmental parameters and mature TC parameters taken from our numerical simulations below (section 3) in tropical conditions. We take ambient surface pressure p_a = 1015 hPa, sea surface temperature SST = 300 K, air–sea temperature difference ΔT = 1 K (thus T_s = SST − ΔT = 299 K), environmental near-surface relative humidity $\mathcal{H}_e$ = 0.9 (thus p_{da} = 985 hPa), the outflow temperature T_o = 200 K, Coriolis parameter $f = 5 \times 10^{-5}$s^{-1}, the maximum wind of the TC $V_{\rm max}$ = 83 m s^{-1}, radius of maximum wind r_m = 64 km, and TC outer radius r_a = 2193 km. Note that the specific value taken for r_a is simply to be consistent with idealized simulations of a TC and it is the same as the value obtained in section 2c. We take two tunable parameters η = 1/2 and β = 5/4 as discussed above. We also take the limit of $r_o = +\infty$. With these parameters, we have A = 0.062, B = 0.031, and C = 0.008. The two curves represented by the lhs and rhs of Eq. (16) are shown in Fig. 2. We note that there are two roots for Eq. (16) with the given values of parameters. One is 1.081, and the other is ~18. The red line [lhs of Eq. (16)] in Fig. 2 can be interpreted as the actual work performed in the boundary layer, and the blue curve [rhs of Eq. (16)] is interpreted as the available work to be performed in the boundary layer. Thus, we observe that the smaller root corresponds to a physically stable state of a TC while the larger root corresponds to an unstable state (see also Emanuel 1988). Thus, here and hereafter, we take the smaller root of Eq. (16) for the dry air partial pressure drop determined by the updated Carnot cycle. The smaller root y = 1.081, which corresponds to an 8.1% surface dry air pressure drop, gives $p_m = p_{dm} + e_s^*$ = 944 hPa, which is a reasonable value as will be seen in simulations later.

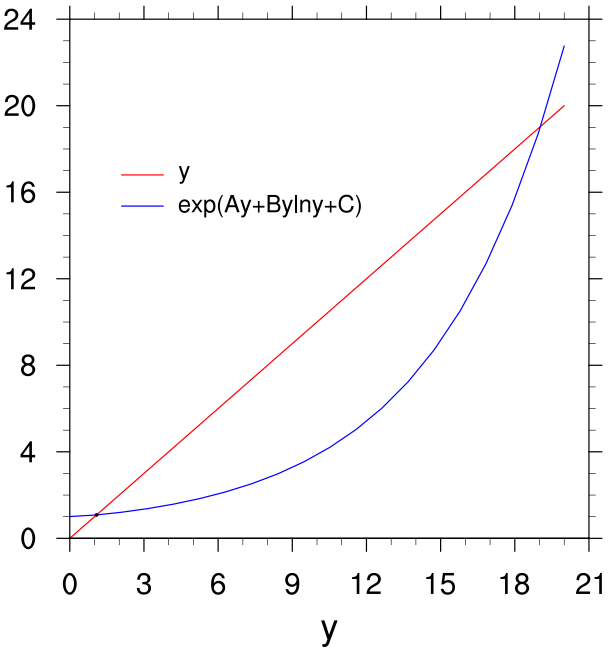

FIG. 2. A representative example of how the roots of Eq. (16) are obtained. Here $A = 0.062$, $B = 0.031$, and $C = 0.008$. See text for more details.

One notable property of the solution for p_{dm}, which will be necessary to understand the TC PS predictions below, is that increasing A (e.g., via increasing T_s) will decrease the Carnot prediction of p_{dm}, while decreasing C (e.g., via increasing r_a) will increase the Carnot prediction of p_{dm}.

We note that the Carnot model assumes the loss of M in the inflow is restored solely in the upper troposphere by some turbulent mixing. The maximum anticyclonic wind speed will be $\sim (1/2)fr_a$, giving tens of meters per second. Previous studies show that though the near-surface flow beyond r_a can exhibit anticyclonic flow, the wind speeds are quite small (CE14; Cronin and Chavas 2019), indicating that much of the M is restored in the free troposphere. Thus, the outflow work term in the Carnot cycle model is a reasonable though highly idealized representation of this process.

b. A brief review of C15 model

The C15 complete wind profile model numerically merges the inner-core structure model of ER11 and the outer-region structure model of Emanuel (2004, hereafter E04). The input parameters of the C15 model are outer radius r_a, maximum gradient wind V_{gm}, lower-tropospheric subsidence velocity in the subsidence region w_{cool} (positive downward), the surface exchange coefficients of enthalpy C_k and momentum C_d and Coriolis parameter f. The C15 model yields the tangential (gradient) wind profile V as a function of radius r, including radius of maximum wind r_m. Following Wang and Lin (2021), it is convenient to use a nondimensionalized C15 model, where V is nondimensionalized by V_{gm} and r is nondimensionalized by r_a. Thus, we have nondimensional wind $\tilde{V} = V/V_{gm}$ and nondimensional radius $\tilde{r} = r/r_a$. The nondimensional ER11 and E04 model may be written, respectively:

$$\left(\frac{\frac{2V_{gm}}{fr_a}\tilde{r}\tilde{V} + \tilde{r}^2}{\frac{2V_{gm}}{fr_a}\tilde{r}_m + \tilde{r}_m^2}\right)^{2-C_k/C_d} = \frac{2(\tilde{r}/\tilde{r}_m)^2}{2 - (C_k/C_d) + (C_k/C_d)(\tilde{r}/\tilde{r}_m)^2}, \tag{20}$$

$$\frac{\partial(\tilde{r}\tilde{V})}{\partial\tilde{r}} = \frac{C_d V_{gm}}{w_{\text{cool}}}\frac{2\tilde{r}^2\tilde{V}^2}{(1-\tilde{r}^2)} - \frac{fr_a}{V_{gm}}\tilde{r}. \tag{21}$$

Equation (20) indicates that the ER11 model is determined by three nondimensional parameters: $V_{gm}/(fr_a)$, $\tilde{r}_m$, and C_k/C_d. Equation (21) indicates that the E04 model is determined by two nondimensional parameters: $V_{gm}/(fr_a)$ and $C_d V_{gm}/w_{\text{cool}}$. Matching Eqs. (20) and (21) requires three of the four parameters to be externally defined leaving one parameter, $\tilde{r}_m$ in our case, to be internally determined. The nondimensional wind profile $\tilde{V}(\tilde{r})$ can be reduced to $V(r)$ given V_{gm} and r_a. By gradient wind balance, one can obtain p_m and the whole surface pressure profile given environmental near-surface pressure p_a (Chavas et al. 2017). Following ER11, Bister and Emanuel (1998), and Rousseau-Rizzi and Emanuel (2019), V_{gm} may be predicted solely from environmental parameters by

$$V_{gm}^2 = V_p^2 \cong \frac{C_k}{C_d}\frac{T_s - T_o}{T_o}(k_0^* - k_a), \tag{22}$$

where V_p is the potential intensity, k_0^* the ambient saturation enthalpy at SST, and k_a the ambient near-surface enthalpy at T_s.

c. A TC PS model combining C15 and updated Carnot cycle model

The updated Carnot cycle model predicts p_m given environmental parameters T_s, T_o, p_a, $\mathcal{H}_e$ (for calculation of p_{da}), f, and TC intensity/structure parameters $V_{\max}$, r_m, and r_a. The C15 model predicts p_m given environmental parameters SST, T_s, T_o, p_a, w_{cool}, f, C_d, C_k, $\mathcal{H}_e$ (for the calculation of V_{gm}), and TC structure parameter r_a. For the updated Carnot cycle model, $V_{\max}$ may be related to environmental parameters by introducing a coefficient γ_{sg} for supergradient wind so that

$$V_{\max} = \gamma_{sg} V_{gm}, \tag{23}$$

where γ_{sg} may be taken as 1.2 to match simulated TCs [also within the range of 1.1–1.25 found by Kepert and Wang (2001)]. Note that $V_{\max}$ (or V_{gm}) need not be tied to V_p but can be defined as any value, as done in the analytic tests and axisymmetric simulations below to allow for the role of radial turbulence in modifying simulated $V_{\max}$.

Hence, with the environment specified, the C15 model prediction for p_m requires only the overall storm size r_a. Similarly, the updated Carnot cycle predicts p_m given r_a, $V_{\max}$, and r_m, where $V_{\max}$ is provided by Eq. (23) and r_m is provided by C15 model. Hence, to predict p_m from the C15 and updated Carnot cycle models, the only external parameter not defined environmentally is outer storm size r_a. Moreover, p_m

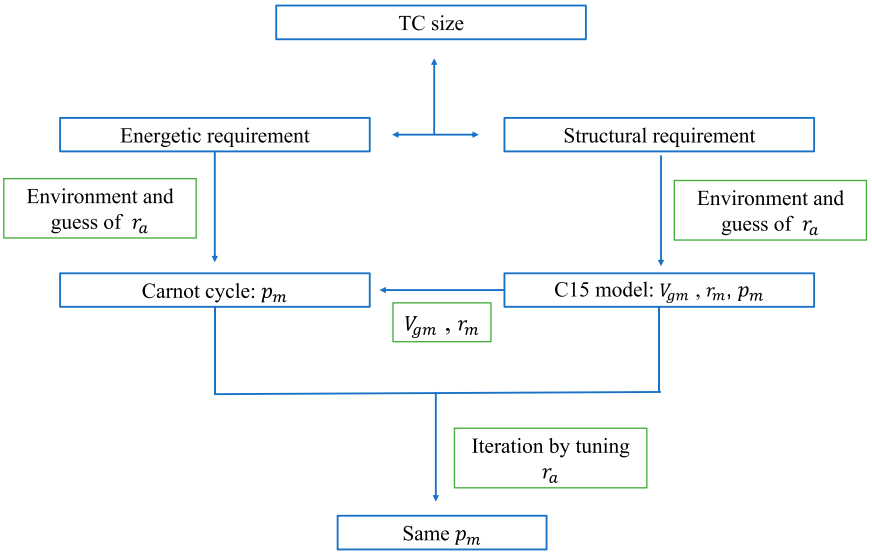

FIG. 3. A schematic summary of the basic idea of TC PS model. Blue boxes and arrows show logic and submodels and green boxes show necessary steps in the iterative solution.

predicted by the updated Carnot cycle is larger with larger r_a (Emanuel 1991), while p_m predicted by the C15 model is smaller with larger r_a (Chavas et al. 2017). Thus, there will be a specific r_a that allows p_m predicted by both models to be equal—this specific r_a is the TC PS in a given environment.

Physically, the characteristic wind structure of the TC (C15 model) would predict a lower inner-core pressure as r_a increases by gradient wind balance, but the pressure drop experienced by inflow parcels is limited by its energetic cycle (updated Carnot cycle model). The potential pressure drop is reduced as r_a increases, which prevents infinite expansion of the TC (also discussed in CE14). The above logic is the basic hypothesis of the TC PS model that we present here. A schematic summary of the TC PS model is shown in Fig. 3. The model itself is applied by numerically converging iteratively to the solution for r_a that satisfies both constraints in a given environment.

Taking the parameter settings in section 2a with $w_{\text{cool}} = 0.002$ m s^{-1}, $\mathcal{H}_e = 0.9$, $\gamma_{sg} = 1.2$, and $r_o = +\infty$, Fig. 4a illustrates how the method would yield a unique solution for r_a in a given environment. We test r_a over a range of values from 200 to 5000 km and find the solution for both models that yields the same p_m for each case. With all other parameters held fixed, increasing r_a causes the C15 model to predict a monotonically decreasing p_m through gradient wind balance. Meanwhile, increasing r_a causes the updated Carnot cycle model to predict a monotonically increasing p_m through increasing the work done in the outflow. Thus, there is a single unique solution that satisfies both models, given by $r_a = 2193$ km, with $p_m = 944$ hPa (Fig. 4a). As noted earlier, the TC PS represents the equilibrium *upper bound* on TC size and hence is expected to be larger than typical TC sizes on Earth. Indeed, the observed median TC outer size is ~900 km and the vast majority of TCs are substantially smaller than the traditional upper-bound scaling V_p/f (Chavas et al. 2016). Observations further suggest that the largest TCs do scale with V_p/f over a reasonable range of values of this length scale from 800 to 1600 km (their Fig. 5c). As a specific example, Super Typhoon Tip (1979) was observed to produce a radius of 15 m s^{-1} surface winds over 1100 km during its mature stage (Dunnavan and Diercks 1980); thus, it is plausible that Tip could have an outer radius ~2000 km.

The behavior of the updated Carnot cycle model is understood through Fig. 4b. Increasing r_a only affects parameter C in Eq. (16). As r_a increases, $f^2 r_a^2$ significantly increases and C significantly decreases. By Eq. (16), p_m increases. Physically, increasing r_a causes W_{out} to increase, leaving less energy available for W_{PBL} (Fig. 4b), which directly links p_m through Eq. (12). When r_a is over ~3000 km, W_{PBL} becomes negative. This outcome indicates that there is zero work available to power the near-surface circulation, and hence, an equilibrium TC cannot exist (i.e., zero surface pressure drop) at such sizes under the given environment. Q_s gradually decreases as r_a increases (Fig. 4b), caused by an increasing p_{dm} through Eq. (6). Q_{Gibbs} is approximately constant as r_a increases (Fig. 4b).

Back to Fig. 4a, a further physical interpretation of how TC size is determined may be provided. The interpretation is based on results from idealized simulations (section 3; also Martinez et al. 2020) and in nature (Maclay et al. 2008) that TCs typically continue to expand slowly (r_a increases) after its intensification. We assume the C15 wind structure model is valid at all stages (C15). Thus, we may define the value of p_m predicted by the C15 model as the present p_m. On the other hand, the value of p_m predicted by the Carnot cycle model is interpreted as the potential p_m if the TC were to maintain its present r_a. When the potential p_m is smaller than the present p_m (small but intense TC), there is more energy available for W_{PBL} (gray line in Fig. 4b above zero) and thus the TC may deepen and expand, because for most circumstances the only way a TC decreases its present p_m is by expansion (note that the model assumes intensity is determined solely from the environment). As the TC expands, the present p_m decreases and

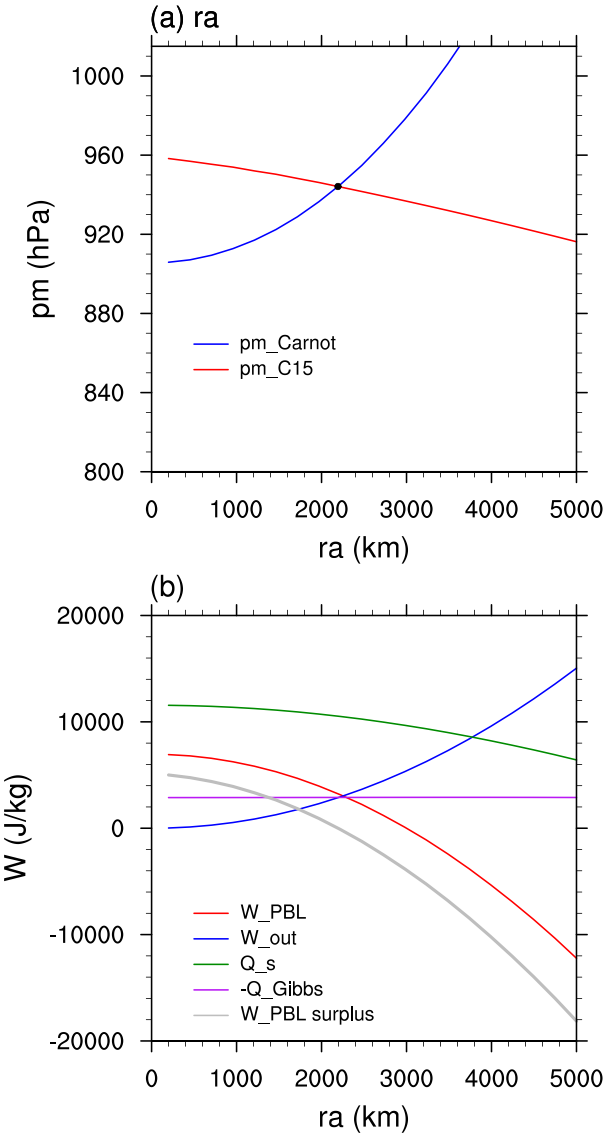

FIG. 4. An example of how TS PS model predicts a specific r_a in a given environment. (a) p_m (hPa) predicted by updated Carnot cycle (blue) and by C15 model (red) with different r_a (km). The intersection point marks the specific r_a and p_m predicted by TC PS model. (b) Different terms (J kg^{-1}) in the updated Carnot cycle model with different r_a. The gray line shows the difference of W_{PBL} (J kg^{-1}) between Carnot model and C15 model.

the potential p_m increases as more work has to be done in the outflow, until a specific size is reached when the present p_m and the potential p_m are equal. Further expansion ceases above this equilibrium size, as the available energy for W_{PBL} would be less than the present value (gray line in Fig. 4b below zero) and as a result the TC would shrink back down—hence, it is a stable equilibrium. Note that this "surplus available work" argument is the energetic explanation for intensification theory ($V_{\max}$) in Tang and Emanuel (2010, 2012); in our case the argument is that if $V_{\max}$ cannot change, then the extra work can be used for expansion rather than intensification.

d. An intrinsic length scale

We next demonstrate that an intrinsic TC PS length scale, V_{Carnot}/f, emerges from a simplified version of the updated Carnot and C15 model equations. The surface pressure deficit corresponding to C15 model may be approximated by (Chavas et al. 2017)

$$p_{da} - p_{dm} = p_{da}(1 - 1/y) \approx DV_{gm} + Efr_a + F, \tag{24}$$

where D, E, and F are regression constants. The updated Carnot cycle model [Eq. (16)] may be linearized (neglecting the B term) by

$$y \approx (1 + C)/(1 - A), \tag{25}$$

noting that $\ln y \approx y - 1$ [similar to Eq. (24) of Emanuel 1986]. Equation (25) also gives an approximate relation $\partial p_{dm,\mathrm{Carnot}}/\partial r_a \sim r_a/y^2$, with $p_{dm,\mathrm{Carnot}} = p_{m,\mathrm{Carnot}} - e_s^*$ (subscript "Carnot" denoting Carnot model predictions).

Eliminating y by combining Eqs. (24) and (25), assuming intensity alone does not have a strong effect on potential size, and making further simplifications (see appendix B) gives a length scale:

$$r_a \sim V_{\mathrm{Carnot}}/f, \tag{26}$$

where V_{Carnot} is defined as

$$V_{\mathrm{Carnot}}^2 = (\eta\epsilon_C L_v - R_v T_s)q_{va}^*, \tag{27}$$

with $q_{va}^* = R/R_v(e_s^*/p_{da})$ the near-surface saturation water vapor mixing ratio of the environment. Here V_{Carnot} is a velocity scale from the updated Carnot cycle. The rhs of Eq. (27) corresponds to the available work of a mixed steam–Carnot cycle (Pauluis 2011) with input latent heat $L_v q_{va}^*$ and input sensible heat $-R_v T_s q_{va}^*$ to a dehydrated parcel.[1] Hence, V_{Carnot} differs from V_p in that V_p reflects air–sea thermodynamic disequilibrium whereas V_{Carnot} reflects the net heat that is obtained in a thermodynamic cycle. V_{Carnot} also lacks a dependence on C_k/C_d. V_{Carnot} may be interpreted physically as the largest possible anticyclonic velocity that can be reached in the outflow at radius r_a of the TC [Eq. (B5)], which is also a physical outcome if all the available mechanical work in the mixed steam–Carnot cycle is used against friction in the outflow [Eq. (B5)].

e. PS model and V_p/f scaling

It is important that the TC PS model should be able to qualitatively reproduce the V_p/f scaling for r_a as found in idealized numerical simulations (CE14). We vary individually f, T_o, and SST (thus T_s) as base cases of varying V_p/f. Varying T_o is by far the cleanest means of varying V_p as it does not alter the thermodynamic structure of the lower troposphere (CE14). Furthermore, we vary C_d and C_k respectively to see if the V_p/f scaling still holds; in this case the thermodynamic properties

[1] A corresponding heating process (with moistening and cooling) will be at constant temperature T_s and constant dry-air partial pressure p_{da} (so that also at constant volume).

(T_o and T_s) in the updated Carnot cycle do not change. Last, we fix all environmental parameters but only vary V_{gm} to see how the TC PS model would predict a size change. This test corresponds to varying the horizonal mixing length in a numerical simulation: past works (Bryan and Rotunno 2009; Rotunno and Bryan 2012; CE14) have shown how increasing the radial mixing length acts to smooth the inner core M field radially outwards, which results in a larger r_m and smaller $V_{\max}$ as $M(r_m)$ stays relatively constant. In the following analysis, other environmental parameters are fixed as in section 2a and 2c. As η is somewhat tunable, we also test the sensitivity of the TC PS model to η for values of 0.4, 0.5, and 0.6. Finally, we test the assumption of $r_o = +\infty$ by taking $r_o = 1.2r_a$ for comparison. We then compare results for V_p/f against the length scale V_{Carnot}/f defined above to examine which length scale best represents equilibrium size.

First, f is varied from 1.25×10^{-5} to 2×10^{-4} s^{-1} and thus $1/f$ is varied from 5×10^3 to 8×10^4 s (Figs. 5a,b). The predicted r_a increases linearly with increasing $1/f$, indicating that the TC PS model correctly yields an f^{-1} scaling. For $\eta = 0.5$ and $r_o = +\infty$, predicted r_a increases from slightly over 500 to ~8700 km. Notably, when $1/f$ is varied, the predicted p_m remains nearly constant, indicating that equilibrium pressure intensity (inner-core surface pressure) does not depend on f. Larger η consistently increases the predicted r_a and decreases the predicted p_m, indicating that a more efficient system yields a larger and deeper storm (with constant maximum wind speed); this behavior will also be seen in later tests. Taking r_o finite (dashed lines) does not change the qualitative behavior but does yield a larger predicted r_a and lower p_m. Physically this response occurs because when r_o is finite, the storm has to do less work in the outflow [Eq. (10)]. This behavior will be seen in later tests as well. Physical explanation of the $1/f$ scaling seen in Fig. 5a is provided in the next subsection.

Second, T_o is varied from 170 to 230 K (Figs. 5c,d). The corresponding V_p varies from ~86 to ~54 m s^{-1}. Overall, the predicted r_a increases with increasing V_p. This is qualitatively consistent with the V_p/f scaling but with a slightly larger magnitude dependence. For $\eta = 0.5$ and $r_o = +\infty$, predicted r_a increases from ~1400 to ~2800 km while V_p/f increases from ~1100 to ~1800 km. V_{Carnot}/f scales closely with V_p/f and hence is also captured by the TC PS model. p_m decreases rapidly with increasing V_p, which is associated with both the increased V_p (thus V_{gm}) and the increased predicted r_a.

Third, SST is varied from 280 to 310 K (Figs. 5e,f). The corresponding V_p varies from ~37 to 96 m s^{-1}, with a proportional increase of 159% for V_p/f. We see a slightly stronger increase of predicted r_a. For $\eta = 0.5$ and $r_o = +\infty$, predicted r_a increases from ~900 to ~3300 km, with a proportional increase of ~267%. V_{Carnot}/f behaves similarly to V_p/f but with a steeper slope (a proportional increase of ~197%), closer to TC PS predictions. Specifically, V_{Carnot} increases from 76.2 to 106.7 m s^{-1} as SST increases from 300 to 310 K, indicating ~4% K^{-1} increase of size or ~60 km K^{-1} at $f = 5 \times 10^{-5}$ s^{-1}. There is also a significant increase of predicted r_a as η increases at constant V_p, as the system is more efficient and the additional power is used to expand the storm. Note the effect is stronger with larger V_p. Similar to varying T_o, we also see a significant decrease of p_m as V_p increases.

The different dependence of r_a on T_o versus SST may be understood considering their quantitatively different roles in the updated Carnot cycle [see Eq. (16)]. While T_o only enters Eq. (16) through ϵ_C, T_s enters Eq. (16) additionally as its own term, and e_s^*.

For our base-case tests, the TC PS model is able to qualitatively reproduce the V_p/f scaling. This indicates that the TC PS model likely captures several important physical processes determining TC size. Next we distinguish V_p/f and TC PS model (V_{Carnot}/f) with two further tests.

Next, we test how TC PS would predict a response of r_a to C_d and C_k, which changes V_p but not V_{Carnot}. Unlike T_o or T_s, C_d and C_k do not influence the thermodynamic property of the system, i.e., through parameter A in Eq. (16), but only influences the parameter C in Eq. (16) by modifying V_p (thus $V_{\max}$). We see from Figs. 6a–d that V_p is varied from ~50 to ~90 m s^{-1}, but the predicted r_a remains approximately constant, even though there is a significant decrease of predicted p_m. We will see that these predictions are also qualitatively consistent with idealized simulations in section 3, indicating that the standard V_p/f scaling is not applicable in this case. Instead, V_{Carnot}/f follows the TC PS predictions.

All together, then, analytical tests suggest that qualitative difference between the TC PS model and V_p/f scaling is mainly the dependence on C_k/C_d. The intrinsic scaling V_{Carnot}/f, independent of C_k/C_d, compares well with TC PS predictions. V_{Carnot}/f also resembles $\sqrt{\chi}/f$, where $\sqrt{\chi}$ is similar to V_p but without the C_k/C_d factor, of previous TC theory (Emanuel 1995) that employs specifically $\sqrt{\chi}/f$ as the relevant nondimensional length scale; note though that dimensional arguments alone cannot determine whether the nondimensional factor C_k/C_d should or should not be included.

Finally, we further test how TC PS predicts a response of r_a to horizontal mixing length l_h in a numerical model. It is known that increasing l_h acts to decrease V_{gm} (Bryan and Rotunno 2009; CE14). Thus, to mimic the effect of l_h, which is not a parameter in either updated Carnot cycle or C15 models, we vary V_{gm} instead. We see from Figs. 6e and 6f that the predicted r_a only slightly decreases as V_{gm} increases, while p_m decreases significantly, which is to be expected from gradient wind balance as the maximum wind speed increases. This is consistent with the observed behavior of TCs in which intensity can vary substantially while the size of the outer circulation remains fixed (Frank 1977; Merrill 1984; Chavas and Lin 2016) and reproduced by the C15 model. Here the TC PS model also predicts that inner-core radial mixing will *not* change outer storm size, and hence, this behavior is both dynamically and energetically consistent. We will also see that these predictions are qualitatively correct in idealized simulations in section 3.

We have also tested the sensitivity of TC PS model to γ_{sg} and β. Predicted r_a increases with a higher γ_{sg} and decreases with a higher β. The former relation is because higher γ_{sg} gives a larger $V_{\max}$ and hence a larger parameter C in Eq. (16), which will shift the blue curves down in Fig. 6 to yield a larger predicted r_a. The latter relation is physically intuitive as a higher water loading is expected to reduce the work available against frictional dissipation, which is related to TC size.

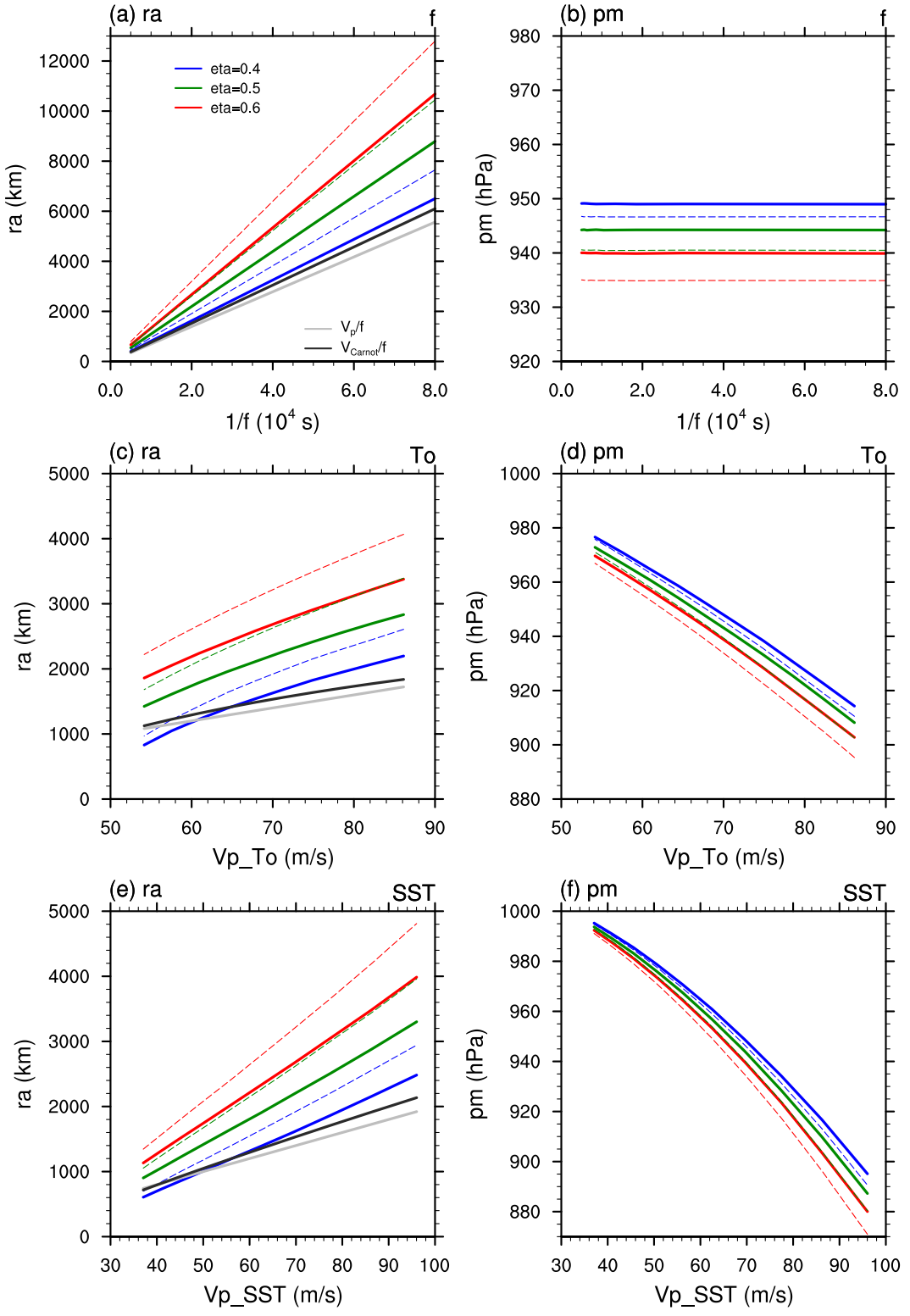

FIG. 5. TC PS model prediction of (left) r_a (km) and (right) p_m (hPa) as (a),(b) f varied from 1.25×10^{-5} to 2×10^{-4} s^{-1}, (c),(d) T_o varied from 170 to 230 K, and (e),(f) SST varied from 280 to 310 K. The x axis is the corresponding $1/f$ (10^4 s) in (a) and (b) and the corresponding V_p (m s^{-1}) in (c)–(f). Predictions with different values of η are in different colors noted by the legend in (a). Thick solid lines are with $r_o = +\infty$ and thin dashed lines are with $r_o = 1.2r_a$. The light gray lines in the left column show V_p/f (km) and the dark gray lines show V_{Carnot}/f (km) with $\eta = 0.5$.

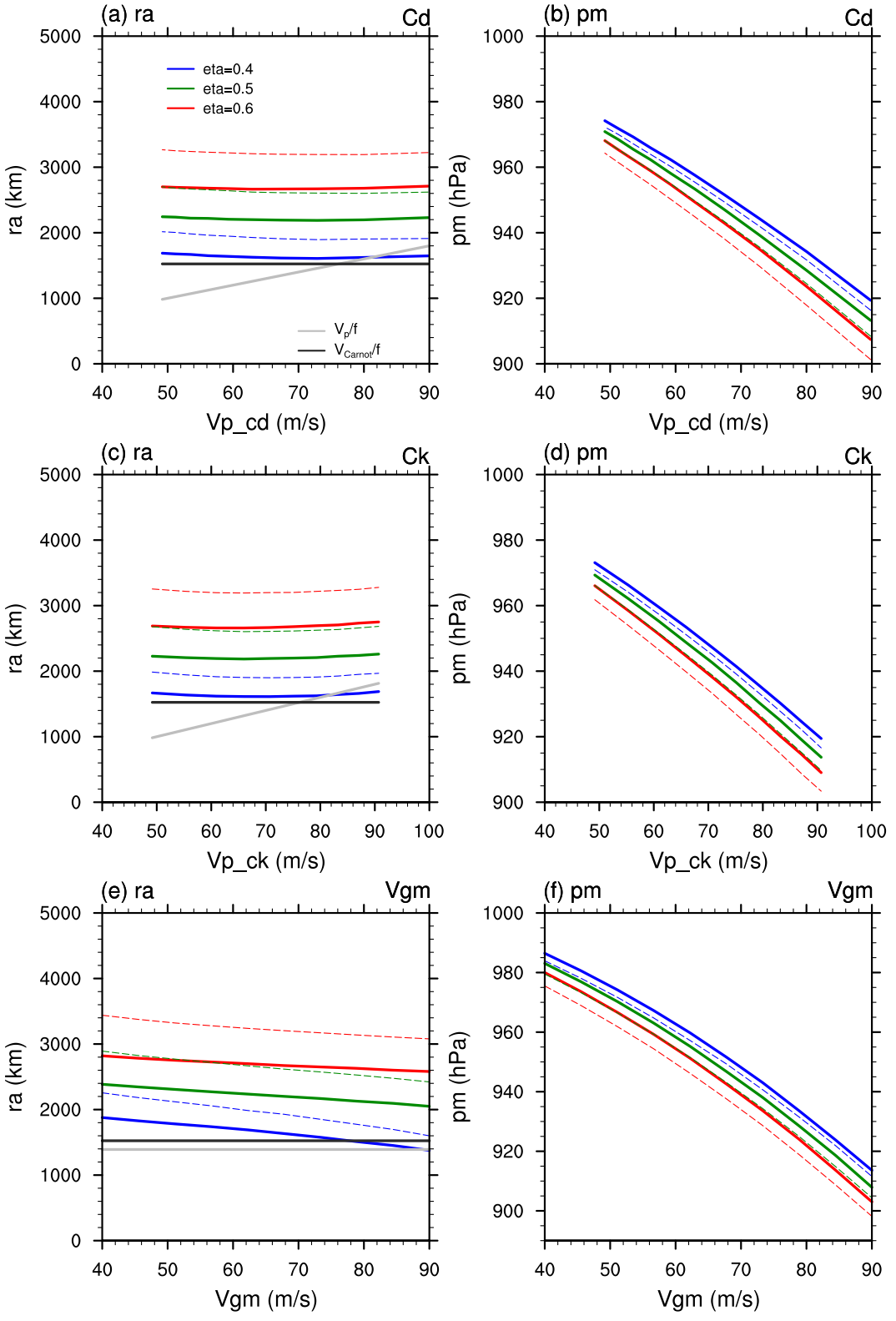

FIG. 6. As in Fig. 5, but with (a),(b) C_d varied from 0.0009 to 0.003, (c),(d) C_k varied from 0.000 75 to 0.002 55, and (e),(f) V_{gm} varied from 40 to 90 m s^{-1}. The x axis is the corresponding V_p (m s^{-1}) in (a)–(d) and the corresponding V_{gm} (m s^{-1}) in (e) and (f).

f. Further understanding of TC PS model results

Details of how the predictions for p_m from both the Carnot cycle and C15 models as r_a is varied yield a single unique solution for the six tests above is shown in Fig. 7. For simplicity, only cases with $\eta = 0.5$ and $r_o = +\infty$ are shown. In each test, the basic responses of p_m predicted by the updated Carnot cycle ($p_{m,\text{Carnot}}$) and C15 model ($p_{m,\text{C15}}$) with increasing r_a are qualitatively the same as Fig. 4a: larger r_a (a larger low-level storm) yields a higher p_m (lower pressure intensity) for Carnot cycle and a lower p_m (higher pressure intensity) for C15 model. However, the final TC PS prediction for the response of r_a in each test is determined in a complicated way: the solution depends on the sensitivity of $p_{m,\text{Carnot}}$ to some parameter (X), $\partial p_{m,\text{Carnot}}/\partial X$, which corresponds to how quickly the blue curve shifts downward as a function of r_a, relative to the $p_{m,\text{C15}}$ sensitivity, $\partial p_{m,\text{C15}}/\partial X$, which corresponds to how quickly the red curve shifts downward as a function of r_a. When $\partial p_{m,\text{Carnot}}/\partial X > \partial p_{m,\text{C15}}/\partial X$, the PS will typically decrease (Figs. 7a,b). When $\partial p_{m,\text{Carnot}}/\partial X < \partial p_{m,\text{C15}}/\partial X$, the PS will typically increase (Fig. 7c). When $\partial p_{m,\text{Carnot}}/\partial X = \partial p_{m,\text{C15}}/\partial X$, then the PS will not change (Figs. 7d–f).

When f is varied (Fig. 7a), we observe that $p_{m,\text{C15}}$ decreases faster with r_a as f increases. This directly corresponds to gradient wind balance. Correspondingly, $p_{m,\text{Carnot}}$ increases faster with r_a as f increases. This is solely a reflection of the increase of parameter C in Eq. (16). Note that parameter A and B are constant when f is varied. The $r_a \sim 1/f$ scaling is produced by the fact that f and r_a only appear as their product fr_a in the TC PS model if M_m is neglected and assuming r_o approaches infinity (appendix B). Thus, the TC PS model is invariant when $r_a \sim 1/f$. The final outcome is the prediction that p_m will remain constant as f is varied [Eqs. (24) and (25)].

Comparing Figs. 7b and 7c, varying T_s has a larger impact on $p_{m,\text{Carnot}}$ than varying T_o. Increasing T_s directly increases the potential of heat received in the inflow [Eq. (6)] by increasing e_s^* and the net heat in the cycle by increasing ϵ_C, whereas decreasing T_o only increases ϵ_C. The same is also seen in V_{Carnot}.

The budget terms from Eq. (5) in the updated Carnot cycle for each of the six TC PS model tests are shown in Fig. 8. When varying f (Fig. 8a), Q_s, Q_{Gibbs}, and W_{PBL} are approximately constant because p_m is approximately constant and V_p (thus V_{gm}) is constant. Thus, from Eq. (5), W_{out} (and fr_a) must remain approximately constant too. For tests varying T_o and T_s, W_{PBL} and W_{out} both increase with V_p (Figs. 8b,c), which is associated with a decrease of p_m and increase of r_a. Comparing Figs. 8b and 8c, T_s has a larger impact on Q_s than T_o. For tests varying C_d, C_k, and V_{gm} (Figs. 8d–f), W_{PBL} increases with V_p and V_{gm}, respectively, because of the decrease of p_m; W_{out} is found to have similar variation as r_a. Q_{Gibbs} is approximately constant except for variations in T_s that induce substantial increases in water mass loading with warming.

3. Evaluation of the TC PS model against idealized numerical simulations

a. Model configuration and experimental design

The numerical model used is Cloud Model 1 (CM1; Bryan and Fritsch 2002) release 19.2, which has three-dimensional (3D) and axisymmetric configurations for idealized simulations. We use a 3D configuration in a small domain without background rotation to obtain a radiative–convective equilibrium (RCE) state, which is then taken as the base state for TC simulations using axisymmetric configuration with background rotation, similar to the approach of CE14. The following model settings are the same for 3D and axisymmetric simulations, except otherwise noted. The horizontal resolution is 4 km and the vertical resolution is 100 m below 3 km of altitude and stretches gradually to 500 m at 12 km of altitude and remains constant above this altitude. The domain height is 25 km. The microphysics scheme is the Morrison double-moment scheme (Morrison et al. 2005). Turbulence is parameterized for mesoscale modeling with horizontal mixing length l_h set to 1500 m and asymptotic vertical mixing length set to 100 m. A Rayleigh damping zone is applied in the upper 3 km of altitude for both 3D and axisymmetric simulations and the outer 100 km of radius for axisymmetric simulations. To effectively control the tropopause temperature T_{tpp}, which approximates T_o, radiation is represented using a simple constant cooling scheme following Chen and Chavas (2020). T_{tpp} is given as an external parameter. When temperature T is higher than T_{tpp}, then a constant cooling rate Q_{cool} (defined positive here) is applied to the potential temperature θ; otherwise, θ is relaxed to the corresponding value to T_{tpp} with a relaxation time τ, i.e.,

$$\frac{\partial \theta}{\partial t} = \begin{cases} -Q_{\text{cool}}, & T > T_{\text{tpp}}, \\ \dfrac{\theta(p, T_{\text{tpp}}) - \theta(p, T)}{\tau}, & T < T_{\text{tpp}}. \end{cases} \tag{28}$$

Here Q_{cool} is set to 1 K day^{-1} and τ set to 12 h.

The surface fluxes are calculated using the classic aerodynamic formulas with constant surface exchange coefficient for momentum C_d and enthalpy C_k. Following CE14, a "background" wind speed u_{sfc} is added as a modification to the surface-flux calculations to represent the enhancement of surface fluxes from unresolved gustiness. The surface enthalpy flux F_k and surface stress $\boldsymbol{\tau}_s$ are thus formulated as

$$F_k = C_k \rho_d (|\mathbf{u}| + u_{\text{sfc}})(k_0^* - k), \tag{29}$$

$$\boldsymbol{\tau}_s = C_d \rho_d (|\mathbf{u}| + u_{\text{sfc}})\mathbf{u}, \tag{30}$$

where ρ_d is the near-surface dry-air density, $\mathbf{u}$ the near-surface horizontal wind vector, and $|\mathbf{u}|$ the near-surface horizontal wind speed. Equations (29) and (30) are applied to all 3D and axisymmetric simulations, with u_{sfc} set to 5 m s^{-1}.

We define our Control experiment (CTL) with the following parameters: $T_{\text{tpp}} = 200$ K, SST = 300 K, $f = 5 \times 10^{-5}$ s^{-1}, $C_d = C_k = 0.0015$, and $l_h = 1500$ m. The initial vortex in CTL is defined following Eq. (37) of Rotunno and Emanuel (1987).

We conduct six sets of axisymmetric TC experiments (Table 1) corresponding to section 2d, with each set varying f (Ex_F), T_{tpp} (Ex_TTPP), SST (Ex_SST), C_d (Ex_CD), C_k (Ex_CK), and l_h (Ex_LH), respectively. The initial vortices are the same as in CTL. For Ex_TTPP and Ex_SST, the base state is defined from their corresponding 3D RCE states. For

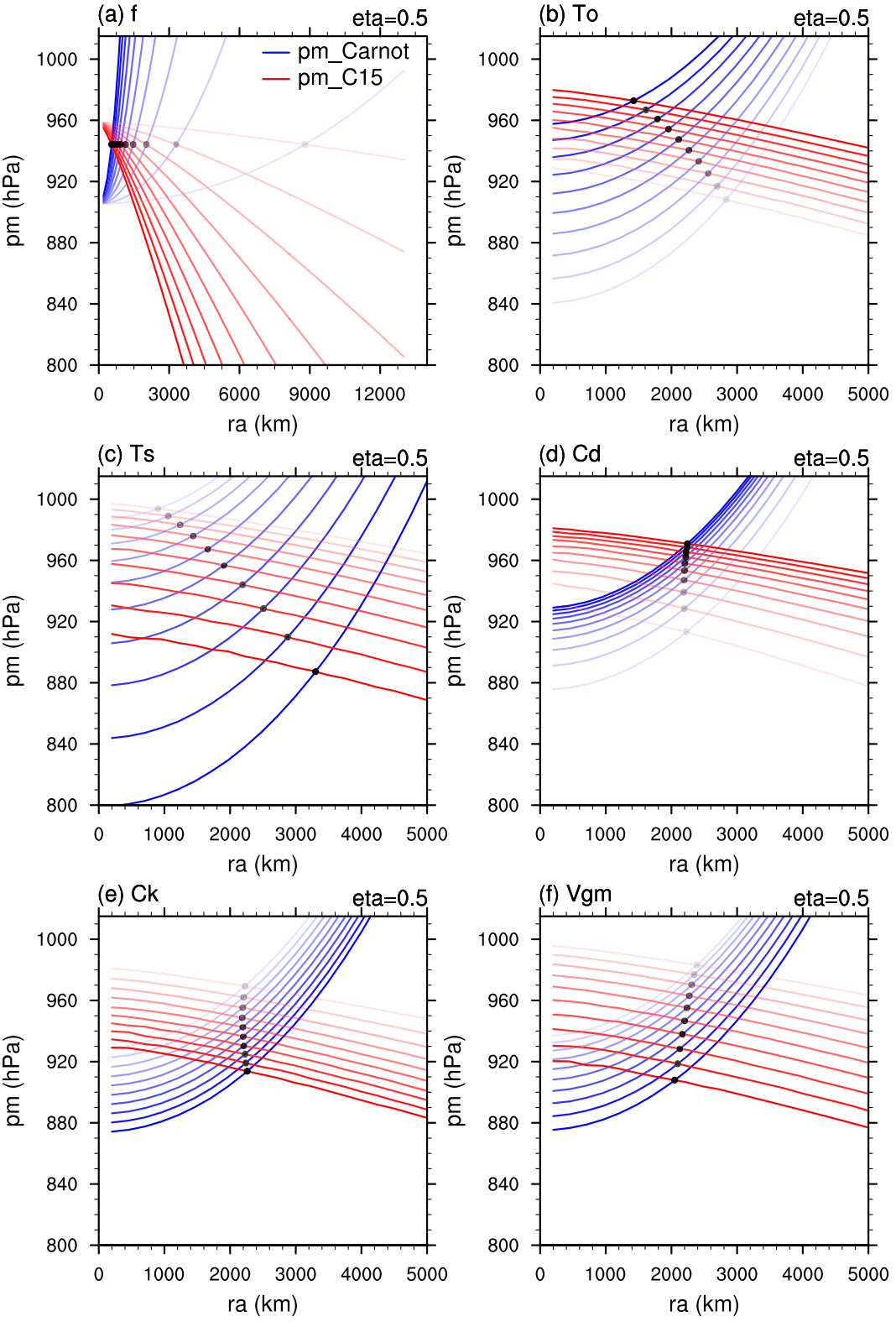

FIG. 7. p_m predicted by the updated Carnot cycle model (blue) and the C15 model (red) over a range of values of r_a induced by variations in (a) f, (b) T_o, (c) T_s (SST), (d) C_d, (e) C_k, and (f) V_{gm}. We set $\eta = 0.5$. More opaque line means higher values of the variable varied. The TC PS–model-predicted p_m and r_a are intersections of blue and red curves, marked by black dots.

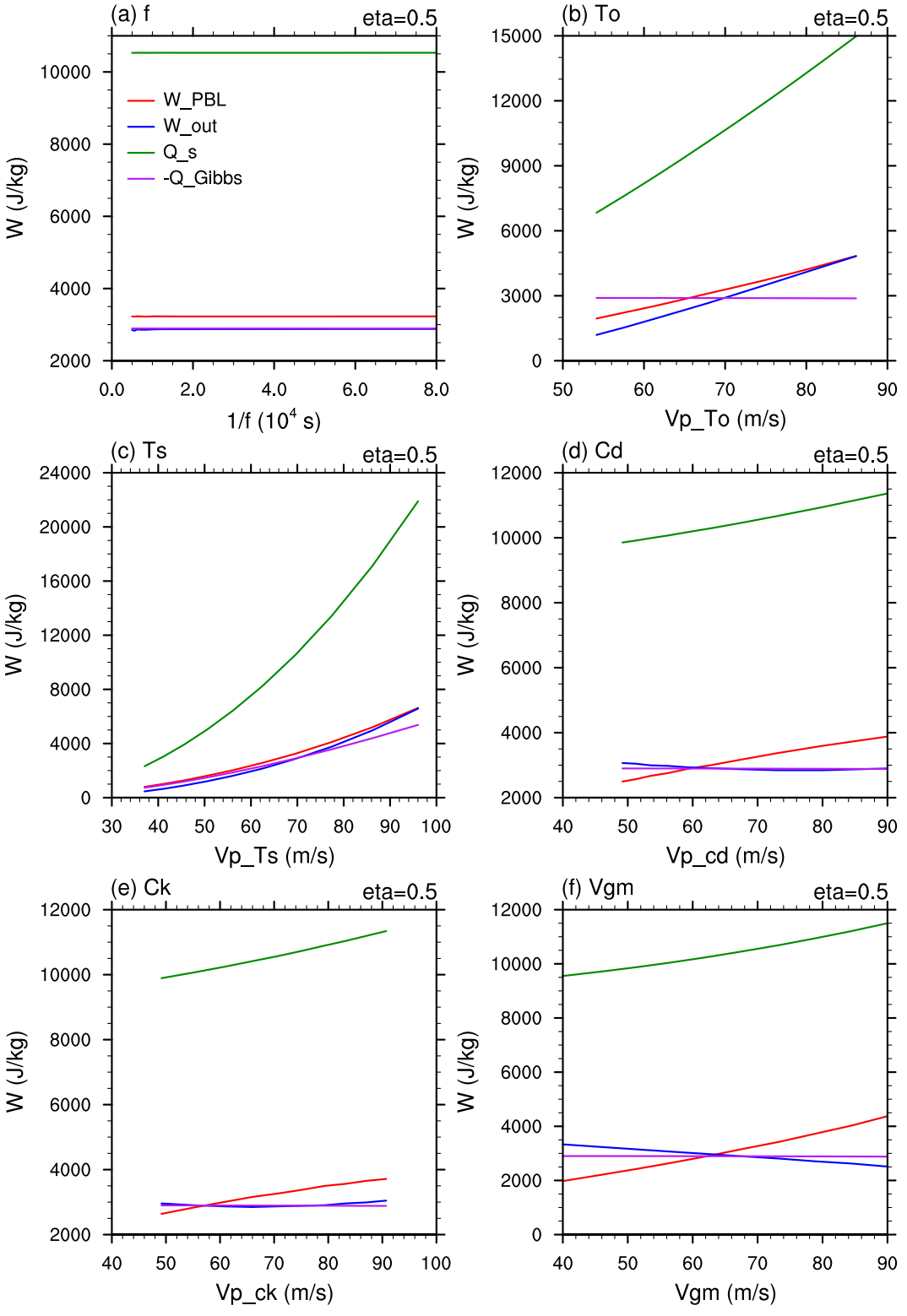

FIG. 8. W_{PBL}, W_{out}, Q_s, and $-Q_{\mathrm{Gibbs}}$ (J kg^{-1}) in the updated Carnot cycle with $\eta = 0.5$ corresponding to the TC PS–model predictions in the six tests where (a) f, (b) T_o, (c) T_s (SST), (d) C_d, (e) C_k, and (f) V_{gm} are varied.

TABLE 1. Experiment sets for the axisymmetric CM1 TC simulations. CTL parameters are shown in boldface.

Ex_F f (10^{-5} s^{-1})	Ex_TTPP T_{tpp} (K)	Ex_SST SST (K)	Ex_CD C_d (10^{-3})	Ex_CK C_k (10^{-3})	Ex_LH l_h (m)
	163		0.9	0.7	
1.25	174	280	1.0	1.0	375
2.5	187	290	1.2	1.2	750
5	**200**	**300**	**1.5**	**1.5**	**1500**
10	214	305	1.9	1.8	3000
20	227		2.3	2.2	6000
	241		3.1	2.5	

other experiments, the base state is the same as the CTL simulation. The 3D simulations are run for 100 days and the average sounding calculated from the last 15 days are used as the base state for axisymmetric TC simulations. The horizontal domain size for 3D simulations is 240 × 240 km^2. The domain height is 25 km for all experiments except 28 km when SST = 305 K and T_{tpp} = 163 K. The axisymmetric TC simulations are run for 100 days in all experiments except 150 days for f = 0.000 012 5 s^{-1} to achieve a sufficiently long quasi-steady state. The domain for TC simulations is 6000 km for all experiments except for cases where TC size is especially large: 8000 km for T_{tpp} = 163 K, 10 000 km for SST = 305 K, and 15 000 km for f = 0.000 012 5 and 0.000 025 s^{-1}.

Time series of TC intensity and sizes in CTL are shown in Fig. 9. After day 30, intensity remains quasi steady within the 100-day period, similar to CE14. Outer size increases rapidly to a peak at approximately 40 days and then fluctuates about a quasi-steady long-term value through 100 days. Thus, a quasi-equilibrium/steady state for tens of days can be reached in our experimental setup. We note that the environment is

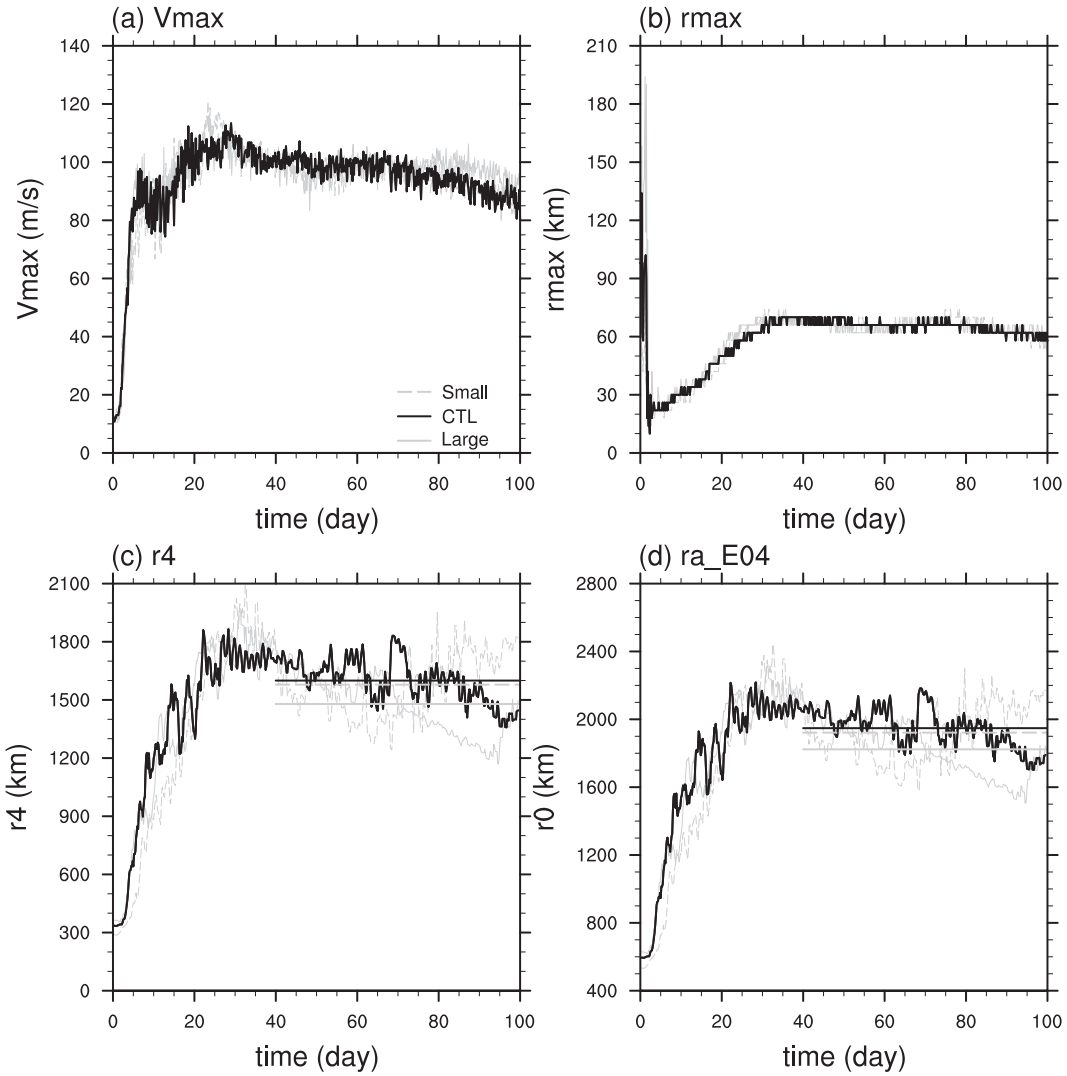

FIG. 9. Time series of (a) V_{max} (m s^{-1}), (b) r_m (km), (c) radius of 4 m s^{-1} tangential wind at 1 km height r_4 (km), and (d) r_a by fitting E04 model to r_4 (see text). In (c) and (d), a 24 h running average has been applied. The horizontal lines in (c) and (d) mark the 40–100 day average values. Solid and dashed gray lines show Large and Small experiments (see text), respectively.

also quasi steady during most of the simulation period after the first few days (not shown) with no additional nudging applied to the environment. Note that the use of constant cooling for representing radiation [Eq. (28)] ensures that deep convection is persistent in the environment to balance this radiative cooling, which resupplies moisture to the free troposphere lost to precipitation. This approach avoids the long-term storm decay that occurs when using Newtonian cooling toward an initial state in the absence of an artificial moisture relaxation (Rousseau-Rizzi et al. 2021).

As the true r_a can be noisy in simulations owing to noise at the very outer edge of the storm, we estimate r_a from r_4, the radius of 4 m s^{-1} tangential wind at 1 km, using the E04 model, which is the outer circulation component of the C15 model. At each output time step (every 4 h), the E04 model is fit to r_4 (see also Fig. 9d), with diagnosed $w_{\rm cool}$, following CE14 from the equation for radiative–subsidence balance:

$$w_{\rm cool} = Q_{\rm cool} \Big/ \frac{\overline{\partial\theta}}{\partial z}, \tag{31}$$

where the overbar denotes time- and area-weighted horizontal radial average and pressure-weighted vertical space average over the steady state (defined below, 40–100 days for CTL) and the outer 900 km (outside the Rayleigh damping zone) of the domain and 1.5–4 km of altitude.

Simulated size is generally larger than those in CE14. This difference may be due to differences in model setup: the different microphysics schemes, difference values of $u_{\rm sfc}$ (3 m s^{-1} in CE14), a coarser vertical resolution in CE14. Additionally, CE14 chose to analyze the wind profile at $z = 1.56$ km, which is likely well above the boundary layer height especially at large radii. As a result, this choice will likely yield a wind profile that decays more quickly with radius in the outer circulation. Our simulations have much higher vertical resolution at low levels and hence we can select a more appropriate height (1 km) for our analysis.

The TC PS model predicts equilibrium outer size from environmental parameters alone, and hence, it should be insensitive to initial vortex size as was found in CE14. We perform two sensitivity experiments (Fig. 9) varying initial r_m (~100 km in CTL) while holding initial intensity unchanged: ~60 km ("Small") and ~140 km ("Large"). Indeed, varying the initial r_m does not induce systematic variations in equilibrium storm properties relative to CTL, particularly when compared to the effects of varied environment (see Fig. 10). Thus, we confirm that equilibrium outer size is largely environmentally defined. Note that initial vortex size can modify storm size within the first few days of the simulation as shown in Martinez et al. (2020) and Tao et al. (2020).

b. *Comparison of TC PS predictions with numerical simulation results*

Based on Fig. 9, steady state is taken as the average of days 40–100 for simulated TCs in all experiments except for two experiments with very small f (days 100–150 for $f = 0.000\,012\,5$ s^{-1} and days 60–100 for $f = 0.000\,025$ s^{-1}). In axisymmetric simulations, V_{gm} is not well constrained by V_p because of a dependence of V_{gm} on l_h (Rotunno and Bryan 2012; CE14). Thus, we use the steady-state average of simulated $V_{\rm max}$ and V_{gm} (by pressure field at the lowest model level) for the TC PS model, which together define γ_{sg} (1.27 for CTL). The value of r_m for M_m is predicted internally by the C15 model.

We define $r_{a,{\rm cm1}}$ as the steady-state average of the estimated outer radius from the E04 model, which we then compare with the TC PS prediction of r_a. Similarly, we calculate steady-state averages of simulated surface pressure at r_m, $p_{m,{\rm cm1}}$, to compare with the TC PS model prediction.

The simulated TCs have a fully developed upper-tropospheric anticyclone core, and thus, we may retain the term $-(1/2)(M_a^2 - M_m^2)/r_o^2$ in the calculation of $W_{\rm out}$ [Eq. (19)]. r_o is estimated from simulated values $r_{o,{\rm cm1}}$ in TC PS–model predictions. $r_{o,{\rm cm1}}$ is assumed to be steady-state average of the radius of the maximum anticyclonic wind in the simulations, same as the definition in section 2a. Because the upper-level anticyclone typically extends beyond the surface cyclone, we assume r_o is some factor larger than r_a, i.e., $r_o = (r_{o,cm1}/r_{a,cm1}) \times r_a$ (this factor is ~1.27 for CTL).

We also provide a comparison with the V_p/f scaling. V_p [Eq. (22)] is calculated from the simulations as the steady-state mean of the value calculated from radial mean $k_0^* - k_a$ and radial mean tropopause temperature over the outermost 900 km (excluding the Rayleigh damping zone) of the domain. The corresponding values of V_p in each experiment is shown in Table 2. As in CE14, this is not calculated within the storm inner core (and without any iteration to account for the effect of reduced pressure on enthalpy variables) but instead is calculated from the far-field environment so that it may be considered a purely environmental parameter.

For direct comparison, we define the environmental parameter values in the TC PS model directly from the simulations. Specifically, SST and f are taken as their values in each CM1 experiment and T_o is taken as $T_{\rm tpp}$ in each CM1 experiment. As T_s (near-surface air temperature) is not rigorously defined in the TC PS model, for simplicity we take T_s to be the steady-state mean of radial mean temperature of lowest model level over the outer 900 km (excluding the Rayleigh damping zone) of the domain; p_a and $\mathcal{H}_e$ are obtained in the same manner. Note that $p_a \sim 1013$ hPa in CTL, smaller (larger) when the atmosphere is cold (warm), e.g., ~1004 hPa at SST = 280 K and 1024 hPa at $T_{\rm tpp} = 241$ K. $\mathcal{H}_e \sim 0.88$ in CTL, smaller (larger) when SST (or C_k) is low, e.g., 0.81 at SST = 280 K and 0.91 when SST = 305 K. The temperature difference between SST and T_s decreases from ~1.7 K at SST of 280 to ~0.4 K at SST of 305 K.

For a better fit to simulation results, $\eta = 0.4$ is chosen, which is a slightly lower efficiency than a pure triangle. This likely compensates for the assumption of complete resaturation, which may be too strong of an assumption and thus yields a larger energy input for thermodynamic cycle than that in a simulated TC; such detailed analysis is left for future work. We set $\beta = 5/4$ as was done in section 2. Across all simulations, $r_{o,cm1}/r_{a,cm1}$ is found to be approximately 1.25 and γ_{sg} is found to be approximately 1.27. Note that they are all allowed to vary as given in Tables 3 and 4. The variations of each are necessary for the quantitative match of the TC PS

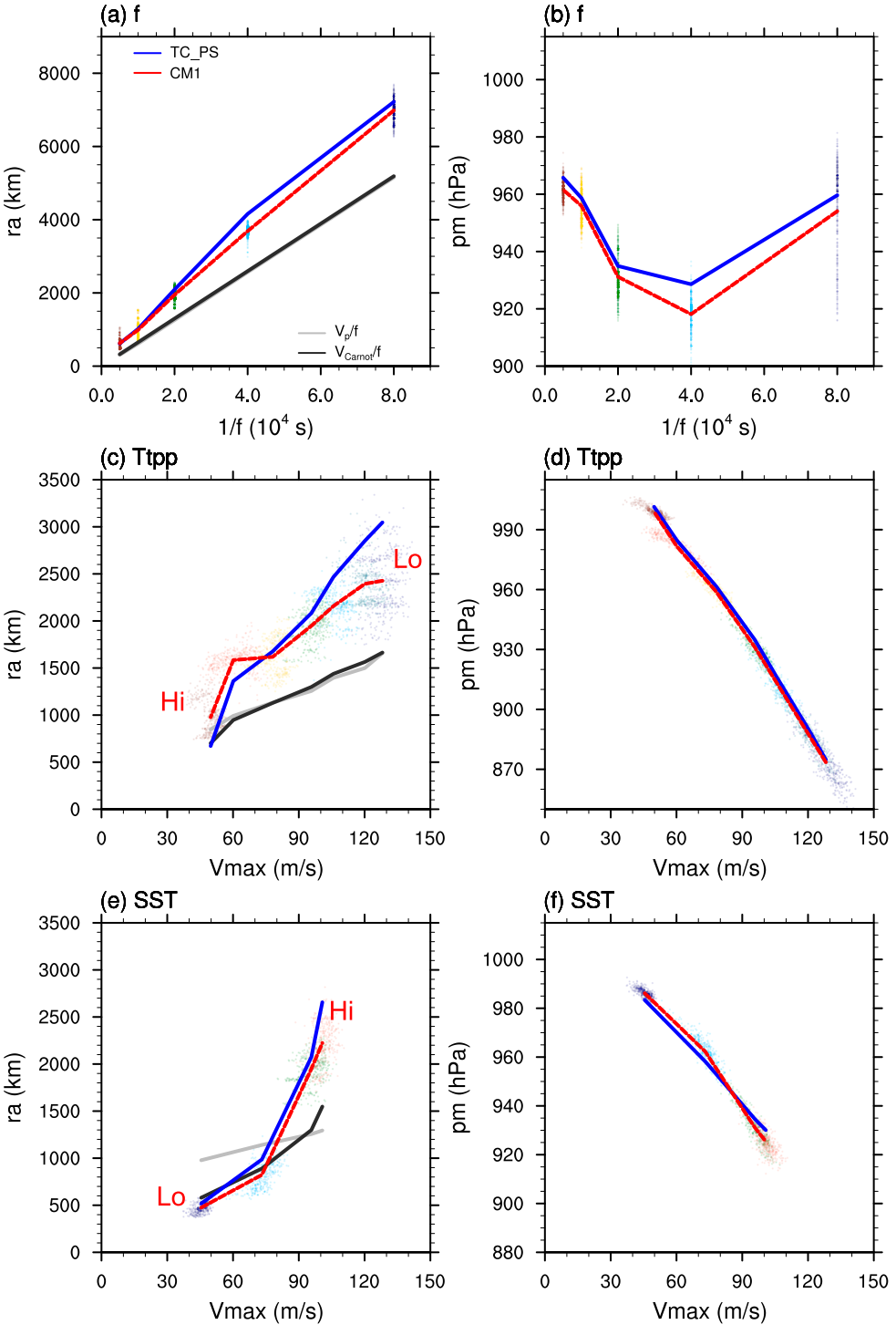

FIG. 10. TC PS–model predictions (blue line) of (left) r_a (km) and (right) p_m (hPa) as a function of V_{max} (m s^{-1}) or $1/f$ (10^4 s) compared to the corresponding steady-state averaged values of CM1 results (red line) for (a),(b) Ex_F, (c),(d) Ex_TTPP, and (e),(f) Ex_SST. Background dots are 4-hourly CM1 output during the steady state. Cold to warm colors mean increased values of the parameter changed in each experiment. The light gray lines in the left column show the corresponding V_p/f (km) and the dark gray lines show the corresponding V_{Carnot}/f (km). "Hi" and "Lo" mark high and low values of the parameter varied, respectively.

TABLE 2. The corresponding V_p (m s^{-1}) in each experiment in Table 1. CTL simulation is shown in boldface. Order of experiments within each set matches that shown in Table 1.

Ex_F	Ex_TTPP	Ex_SST	Ex_CD	Ex_CK	Ex_LH
	82.8		81.5	62.6	
64.4	75.0	48.9	76.8	63.5	62.7
64.1	69.8	57.0	71.5	63.8	64.3
62.8	**62.8**	**62.8**	**62.8**	**62.8**	**62.8**
61.1	56.6	64.7	57.2	64.3	63.0
61.6	49.6		52.0	65.0	61.1
	42.3		45.0	65.2	

TABLE 3. The corresponding $r_{o,\mathrm{cm1}}/r_{a,\mathrm{cm1}}$ in each experiment in Table 1. CTL simulation is shown in boldface. Order of experiments within each set matches that shown in Table 1.

Ex_F	Ex_TTPP	Ex_SST	Ex_CD	Ex_CK	Ex_LH
	1.3		1.3	1.2	
1.3	1.2	1.5	1.2	1.3	1.4
1.3	1.2	1.5	1.4	1.3	1.3
1.3	**1.3**	**1.3**	**1.3**	**1.3**	**1.3**
1.3	1.3	1.4	1.2	1.4	1.2
0.9	1.1		1.3	1.1	1.2
	1.5		1.3	1.3	

model predictions to simulations. The value of w_{cool} is approximately 0.0014 m s^{-1} when SST = 300 K; it increases to 0.003 m s^{-1} when SST = 280 K.

Figure 10 compares TC PS–model predictions of r_a and p_m with corresponding steady-state values of CM1 simulations for the sets of experiments varying f, T_{tpp}, and SST. The TC PS model does well in reproducing the simulated values of both r_a and p_m. The lone quantitative exception is a slightly stronger dependence of TC PS r_a on T_{tpp} than is simulated in Ex_TTPP. V_p/f and V_{Carnot}/f are almost identical for varied f and T_{tpp} and also scale reasonably well with the full TC PS model prediction. For varying SST, V_{Carnot}/f better captures the strong dependence of simulated size on SST than V_p/f. This is because V_{Carnot}/f does not depend on air–sea thermodynamic disequilibrium as V_p/f, so that the increase of environmental relative humidity and decrease of air–sea temperature difference at larger SST, which reduces the air–sea enthalpy disequilibrium, will not influence V_{Carnot}/f.

Figure 11 compares TC PS–model predictions of r_a and p_m with corresponding steady-state values of CM1 simulations for the sets of experiments varying C_d, C_k, and l_h. Equilibrium size does not vary strongly with varying C_d, which is also captured by TC PS model (Figs. 11a,b). For Ex_CK, the air–sea enthalpy disequilibrium decreases as C_k is increased, such that intensity (not shown) and V_p (Table 2) varies only weakly across the experiments in Ex_CK (Fig. 11c). This behavior is consistent with the fact that in RCE surface heat fluxes must balance column radiative cooling (CE14). Since the radiative cooling rate per unit mass is fixed in our setup, if tropospheric mass remains relatively constant then surface heat fluxes must also remain constant; hence, V_p will also remain constant. Importantly, we hold C_k fixed at its CTL value for the ER11 inner-core structure in the TC PS model, which is required to match the simulation results in Ex_CK in Fig. 11. Including variations in C_k in the ER11 model yields an unrealistically small r_m when C_k is small compared to CM1 results, which yields a value of $p_{m,\mathrm{C15}}$ that is too small and hence too small of a potential size. This outcome suggests a possible shortcoming of the C_k dependence in the ER11 model. Results of Ex_LH also confirms that equilibrium size has a very weak dependence on intensity in a fixed environment, which is also captured by the TC PS model.

Overall, when given simulated V_{max} and V_{gm}, the TC PS model does a good job in reproducing the simulated r_a and p_m across all experiments. The V_{Carnot}/f scaling also captures the qualitative variation of simulated r_a across all experiments. Considering the idealization and simplicity of TC PS model, these results demonstrate that the TC PS model captures the essential physical processes that determine equilibrium TC size. The V_{Carnot}/f scaling is similar to V_p/f in reproducing variations in TC PS variation and simulation but better captures variations due to SST and C_d. Finally, we note that V_{Carnot}/f still underestimates the strong dependence of PS on SST, this should result from neglecting the role of r_a in $p_{m,\mathrm{C15}}$, which should be relatively larger when PS is small (appendix B).

4. TC PS model with a simpler Carnot cycle model

In this section, we repeat the same analysis as in section 2e with a simpler Carnot cycle essentially the same as that in Emanuel (1991), and test whether the modifications (half Carnot efficiency, complete resaturation, Gibbs free energy, and work to lift water) to the Emanuel's Carnot cycle are essential to the qualitative TC PS predictions in section 2e.

By neglecting Q_{Gibbs}, W_p, and the energetic effects of remoistening back to environmental relative humidity $\mathcal{H}_e$, and applying a Carnot efficiency ϵ_C to the cycle, we may repeat the same procedure as in section 2a to obtain an expression for y, similar to Eq. (16):

$$y = \exp(A'y + C'), \tag{32}$$

with

$$A' = \frac{\epsilon_C}{1-\epsilon_C}\frac{L_v}{R_v T_s}\frac{e_s^*}{p_{da}}, \tag{33}$$

TABLE 4. The corresponding γ_{sg} in each experiment in Table 1. CTL simulation is shown in boldface. Order of experiments within each set matches that shown in Table 1.

Ex_F	Ex_TTPP	Ex_SST	Ex_CD	Ex_CK	Ex_LH
	1.28		1.21	1.25	
1.11	1.29	1.19	1.22	1.27	1.26
1.27	1.28	1.22	1.24	1.27	1.26
1.27	**1.27**	**1.27**	**1.27**	**1.27**	**1.27**
1.19	1.25	1.28	1.29	1.27	1.24
1.10	1.23		1.32	1.25	1.19
	1.22		1.34	1.26	

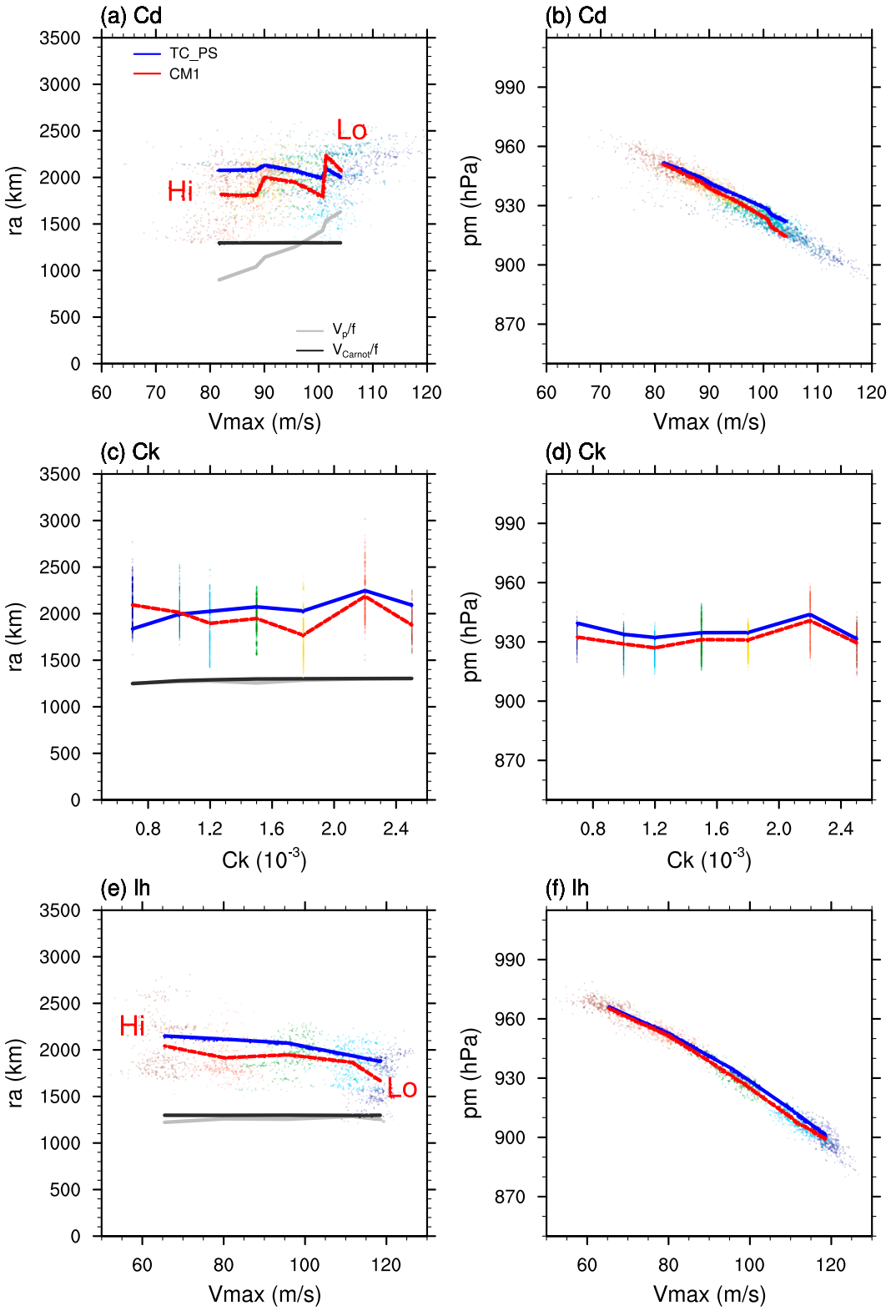

FIG. 11. As in Fig. 10, but for (a),(b) Ex_CD, (c),(d) Ex_CK, and (e),(f) Ex_LH. Note that in (c) and (d), C_k is held to CTL value in TC PS model; see more details in text. Also, the x axis is C_k in (c) and (d) because V_{max} does not separate different simulations in Ex_CK.

$$C' = -\mathcal{H}_e A' + \frac{\epsilon_c}{1-\epsilon_c}\frac{e_s^*}{p_{da}}\mathcal{H}_e \ln\mathcal{H}_e - \frac{1}{(1-\epsilon_c)RT_s} \times \left(-\frac{1}{2}V_{\max}^2 + \frac{1}{4}f^2 r_a^2 - \frac{1}{2}fM_m - \frac{1}{2}\frac{M_a^2 - M_m^2}{r_o^2}\right). \quad (34)$$

Note that in A', there is no $-T_s$ term associated with Q_{Gibbs} and in C' there is an additional $-\mathcal{H}_e A' + C'(\epsilon_c/1-\epsilon_c)(e_s^*/p_{da})\mathcal{H}_e \ln\mathcal{H}_e$ term associated with resaturation of the parcel.

Following a similar procedure in the appendix B, we may obtain a length scale corresponding to the simpler Carnot cycle:

$$r_a \sim V'_{\text{Carnot}}/f, \quad (35)$$

where

$$V'^2_{\text{Carnot}} = \epsilon_C L_v (1-\mathcal{H}_e) q_{va}^*, \quad (36)$$

with $q_{\text{va}}^* = (R/R_v)(e_s^*/p_{da})$. V'_{Carnot} has both features of V_{carnot} and V_p as it combines the net heat in a cycle and environmental relative humidity (contributing to air–sea thermodynamic disequilibrium), though V'_{Carnot} is more similar to V_p. Furthermore, as V'_{Carnot} does not include C_k/C_d, it has an even closer relation with $\sqrt{\chi}$.

Next, we apply the same analysis in section 2e with the same environmental parameters. As we do not have η in the simple Carnot cycle model, we vary γ_{sg} instead, though the physical effects of γ_{sg} and η are not equivalent. Results are qualitatively similar (Figs. 12 and 13) for the six tests as those found in section 2e. A higher γ_{sg} yields a larger predicted r_a and a lower predicted p_m as also discussed in section 2d. The results indicate that none of the modifications to the Emanuel's Carnot cycle as introduced in section 2a is essential to the TC PS model predictions.

However, these modifications do affect the hypercane condition, which refers to the condition where only one or no solutions exist for the Carnot cycle and implies very low inner-core surface pressure. If B term in the updated Carnot cycle is neglected, then the hypercane condition is $1 + \ln A + C \geq 0$ for the updated Carnot cycle, where as it is $1 + \ln A' + C' \geq 0$ for the simple Carnot cycle. Emanuel (1988) suggested a hypercane is possible with SST of 311–313 K. We get a range of 310–313 K for r_a less than ~3400 km if none of the noted modifications are included in the Carnot cycle (Fig. 14), agreeing with Emanuel (1988). This temperature increases to ~327 K for the updated Carnot cycle (Fig. 14), suggesting that the current climate is farther from supporting a hypercane. The result comes from a much lower A than A' (related to half of Carnot efficiency and Gibbs free energy) and a much higher C than C' (related to complete resaturation) in the updated Carnot cycle.

5. Summary and discussion

This study proposed a model to predict tropical cyclone (TC) potential size (PS), i.e., the equilibrium upper-bound outer radius r_a on an f plane, solely from environmental parameters. The TC PS model combines an updated Carnot cycle model, which includes an explicit treatment of the water budget and its energetics as part of the closed cycle, with a physics-based model for the complete radial structure of the wind field. The model yields a deterministic value of the TC outer radius for which both model components yield the same predicted value of the surface pressure under the eyewall (p_m). This model is first tested analytically against V_p/f scaling by varying different environmental parameters and then tested against numerical simulations. A new Carnot cycle–based length scaling is proposed for equilibrium upper-bound TC size. The key findings of our work are as follows:

- Physically, the TC PS is determined as follows: the Carnot model defines how much the pressure can be dropped energetically, and then the C15 model defines, for a given intensity, how large a steady-state storm needs to be to yield that pressure drop.
- Overall, the TC PS model predictions closely match most CM1 simulation results with f, T_{tpp}, SST, C_d, C_k, and l_h varied. This demonstrates that the TC PS model captures the essential physical processes that determine equilibrium TC size on an f plane. Additionally, the TC PS model is able to capture the strong dependence of TC size with increasing SST, and the insensitivity to C_k and C_d, that V_p/f fails to quantitatively capture.
- The $1/f$ scaling of TC PS is produced by the fact that f and r_a (PS) only appear as their product fr_a in the TC PS model; thus, with all other environmental parameters unchanged, TC PS model will be unchanged when $r_a \sim 1/f$.
- The TC PS model suggests a novel Carnot cycle–based scaling V_{Carnot}/f for equilibrium TC size [Eq. (26)]. A fundamental difference between V_{Carnot} and V_p is that V_{Carnot} is based on the net heat in a thermodynamic cycle whereas V_p is based on air–sea thermodynamic disequilibrium. This may explain why V_{Carnot}/f better captures the variation of TC size with SST in CM1 simulations. V_{Carnot}/f suggests a 4% K^{-1} increase of size from SST of 300 to 310 K.
- None of the modifications (half Carnot efficiency, complete resaturation, Gibbs free energy, and work to lift water) to the Emanuel's Carnot cycle is essential to the qualitative behavior of the TC PS model. However, these modifications do yield a much higher critical SST (~327 K) for the hypercane condition than that of the Emanuel's Carnot cycle (~310 K), suggesting that the current tropics is far from supporting a hypercane.
- A simpler Carnot cycle (corresponding to Emanuel's) yields a scaling of V'_{Carnot}/f, where V'_{Carnot} more closely resembles V_p. This may explain why V_p/f can perform well as a scaling for TC size for certain parameters.

One potential significant limitation of the present TC PS model is the assumption of a closed cycle of a parcel in a TC in which the storm restores its own angular momentum. This would inhibit application of TC PS model to real TCs, where

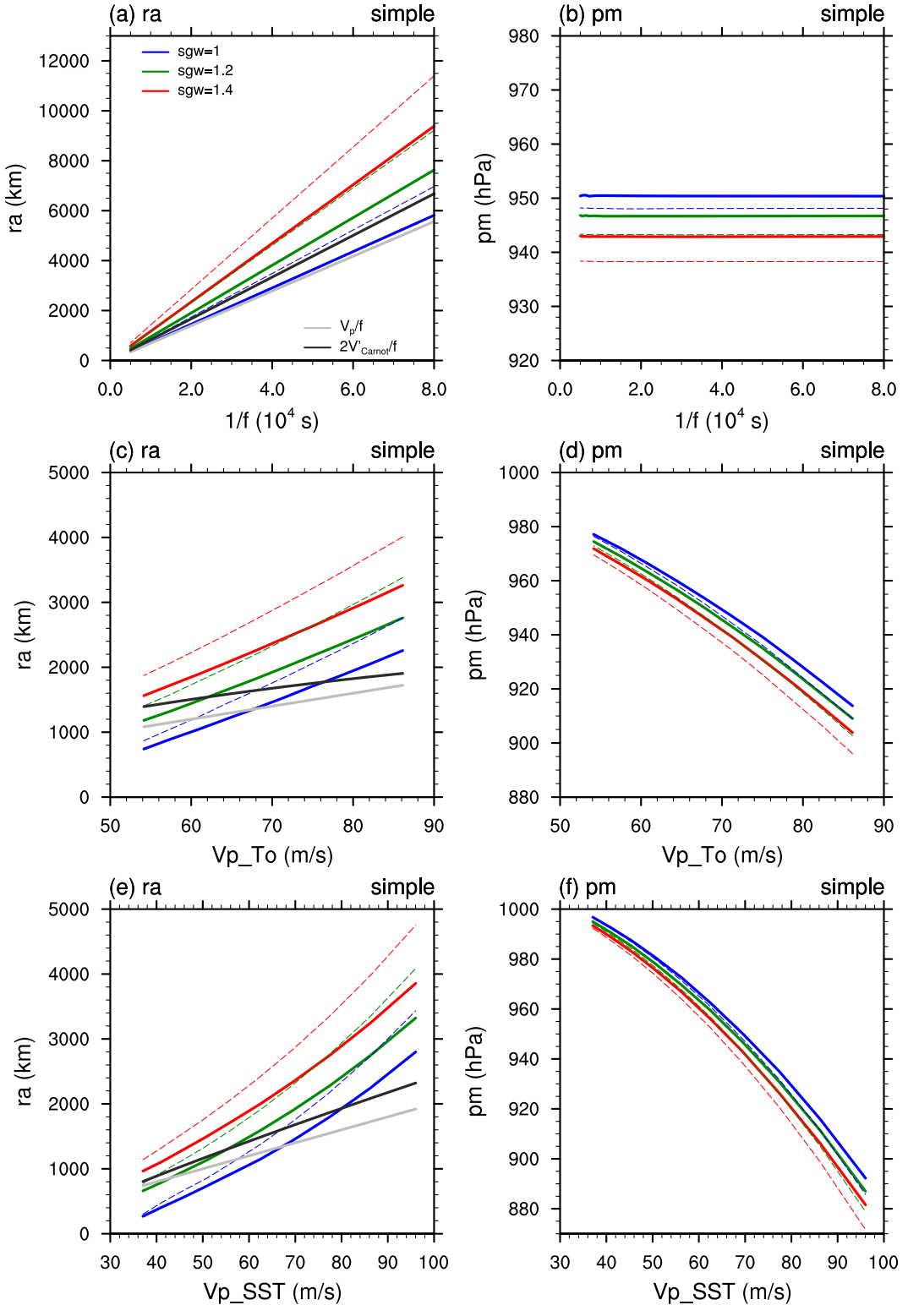

FIG. 12. As in Fig. 5, but for the TC PS model with a simple Carnot cycle. Predictions with different values of γ_{sg} are in different colors noted by legend ("sgw"). The dark gray lines show $2V'_{\text{Carnot}}/f$ (km).

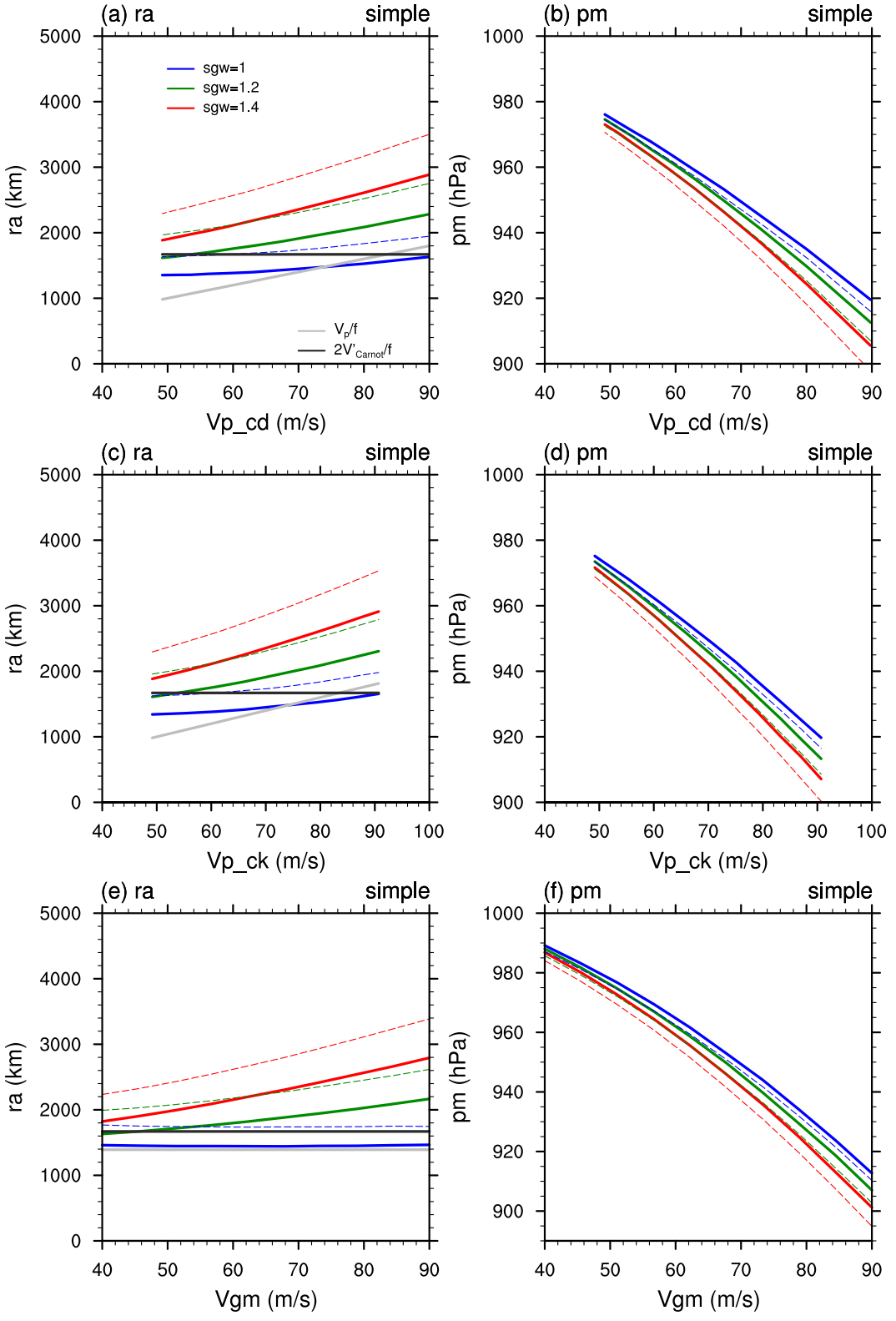

FIG. 13. As in Fig. 6, but for a TC PS model with a simple Carnot cycle. Predictions with different values of γ_{sg} are in different colors noted by legend ("sgw"). The dark gray lines show $2V'_{\text{Carnot}}/f$ (km).

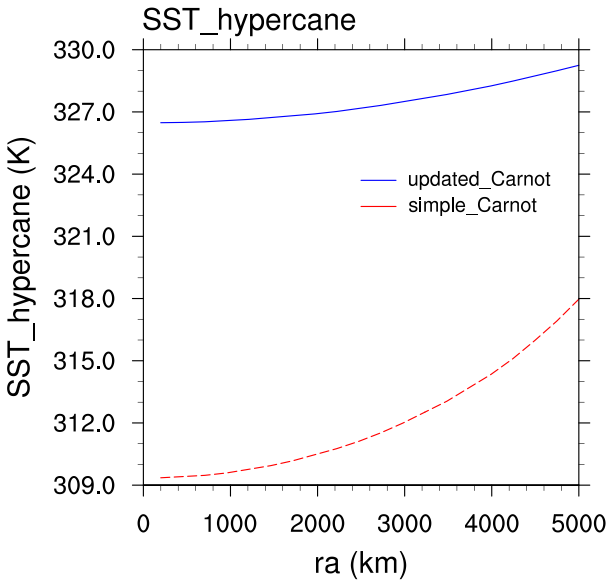

FIG. 14. Critical SST for the hypercane condition as a function of r_a for the updated Carnot cycle (blue) and the simple Carnot cycle (red). In the calculation r_o is taken as infinity and $-(1/2)fM_m$ is neglected in C and C'.

outflow parcels often follow outflow jets that travel far from the storm rather than directly recirculating into the storm in the subsidence region near the outer edge of the storm. However, the fact that the dynamical condition of C15 model also imposes the $r_a \sim 1/f$ scaling, as noted in section 2d, would explain why this scaling does *not* depend on the outflow work term and hence the outflow work term (i.e., the assumption that the storm must restore its own angular momentum) is not essential. Note also that axisymmetry is not strictly required for a Carnot cycle (see section 4 of Emanuel 1988). Examination of how the TC PS model might need to be modified to be applicable to real TCs is an important subject of future work.

A key constraint for equilibrium upper-bound TC size in this study is the outflow work needed to dissipate the kinetic energy of the anticyclone in the upper troposphere. This process introduces f, the inclusion of which has lacked a clear physical basis in previous studies (Khairoutdinov and Emanuel 2013; Emanuel 2022). This outcome emphasizes the need for a better understanding of the descent leg of the cycle, including the processes by which absolute angular momentum is restored in addition to entropy.

Finally, Lu and Chavas (2022) demonstrated using a nondivergent barotropic model that a vortex on a β plane tends to shrink to its vortex Rhines scale as a result of radiation of planetary Rossby waves. The vortex Rhines scale is typically ~200–400 km in their experiments, much smaller than the observed TC outer radius ~ 900 km (Chavas et al. 2016) and the PS ~ 2000 km in the present study. Hence, on the real Earth, the Rhines effect acts as an additional time-dependent sink of kinetic energy that opposes expansion toward the PS. A time-dependent model for TC size that incorporates this effect is a worthy avenue of future work.

Acknowledgments. This work was supported by the National Natural Science Foundation of China (42130603, 41975127). DC was supported by NSF Grants 1945113 and 1826161. The first author thanks Wenchao Chu for maintaining the server on which the simulations were run.

Data availability statement. Description of CM1 model is available at https://www2.mmm.ucar.edu/people/bryan/cm1/. The specific CM1v19.2 model code with the noted modifications and the namelist for CTL simulation used in this study have been uploaded to figshare with DOI: 10.6084/m9.figshare.17134400.

APPENDIX A

Derivation of Eq. (1)

Following Romps (2008), we also define

$$\partial_\alpha(u^\alpha X) = \frac{\partial X}{\partial t} + \boldsymbol{\nabla} \cdot (\mathbf{u}X), \tag{A1}$$

where X is any variable and $\mathbf{u}$ the three-dimensional velocity equivalent to V in Eq. (1). Note with continuity equation $\partial_\alpha(u^\alpha \rho_d) = 0$, a property of Eq. (A1) is $\partial_\alpha(\rho_d u^\alpha X) = \rho_d(dX/dt)$. The kinetic energy equation is given by Eq. (17) of Romps (2008) and may be equivalently written as

$$\partial_\alpha\left[(1+q_t)\rho_d u^\alpha \frac{|\mathbf{u}|^2}{2}\right] = -\boldsymbol{\nabla}\left[\frac{|\mathbf{u}|^2}{2}(\mathbf{d}_v + \mathbf{d}_c)\right] + (1+q_t)\rho_d \boldsymbol{\Gamma} \cdot \mathbf{u} - \mathbf{u} \cdot \boldsymbol{\nabla} p + \mathbf{u} \cdot (\rho_d \mathbf{F}). \tag{A2}$$

Note Romps (2008) worked with specific humidity rather than mixing ratio here. Also note that although Romps (2008) did not include background rotation ($f = 0$), it does not influence the energy equations as Coriolis force is perpendicular to velocity vector and does no work. The potential energy equation may be written:

$$\partial_\alpha[(1+q_t)\rho_d u^\alpha \phi] = \phi \partial_\alpha[(1+q_t)\rho_d u^\alpha] - (1+q_t)\rho_d \boldsymbol{\Gamma} \cdot \mathbf{u}, \tag{A3}$$

where $\partial_\alpha[\rho_d(1+q_t)u^\alpha] = \rho_d(dq_t/dt) = -\boldsymbol{\nabla} \cdot (\mathbf{d}_v + \mathbf{d}_c)$ using continuity equations [see Eqs. (6)–(9) of Romps 2008] with $\mathbf{d}_v$ and $\mathbf{d}_c$ the diffusion (rainfall) fluxes of water vapor and condensates per unit area, respectively. Equation (1) is then obtained by summing Eqs. (A2) and (A3), neglecting the first term on the rhs of Eq. (A2), assuming steady state and using the relation $\partial_\alpha(\rho_d u^\alpha X) = \rho_d(dX/dt)$.

W_p is obtained by integrating the third term on the rhs of Eq. (1) but with a negative sign:

$$W_p = -\oint \phi \, dq_t = \oint q_t \, d\phi = \oint \Gamma q_t \, dz. \tag{A4}$$

APPENDIX B

Derivation of Intrinsic Length Scale

Rearranging Eq. (25) gives

$$1 - \frac{1}{y} = \frac{A + C}{1 + C} \approx A + C. \tag{B1}$$

Substituting Eq. (B1) into Eq. (24) gives

$$(A + C)p_{da} \approx DV_{gm} + Efr_a + F. \tag{B2}$$

As we see in sections 2e and 3b, V_{gm} alone only has a small effect on PS; it is reasonable to assume that all terms associated with V_{gm} in Eq. (B2), i.e., $DV_{gm} + F$, cancel. Thus, we have

$$Ap_{da} - \left\{\frac{1}{4}(fr_a)^2/[(1 - \eta\epsilon_C)RT_s]\right\}p_{da} = Efr_a. \tag{B3}$$

Note M_m has been neglected and r_o taking as infinity in parameter C as well as $\beta = 1$ being used in A and C, meaning M is restored well beyond the storm and the work to lift water is neglected.

Rearranging Eq. (B3) gives

$$\frac{1}{4(1 - \eta\epsilon_C)}(fr_a)^2 + \frac{RT_s}{p_{da}} Efr_a - RT_sA = 0. \tag{B4}$$

To obtain an approximate solution, the second term of Eq. (B4) may be neglected when fr_a is large. This gives a solution:

$$fr_a = 2V_{\text{Carnot}}, \tag{B5}$$

with V_{Carnot} given by Eq. (27). In Eq. (B5) we are neglecting the size effect in C15 model while retaining the V_{gm} effect, merely in order to give a simple solution as it is suggested (Fig. 7) that the quadratic effect of the W_{out} term puts a stronger constraint on TC PS. This approximation will give an overestimation of the PS. Equation (B5) indicates that V_{Carnot} is the anticyclonic velocity that can be reached in the outflow at radius r_a of the TC given M_m negligible compared to $(1/2)fr_a^2$.

A similar procedure to the above but for the simple Carnot cycle in section 4 will give a similar solution:

$$fr_a = 2V'_{\text{Carnot}}, \tag{B6}$$

with V'_{Carnot} given by Eq. (36).

REFERENCES

Bister, M., and K. A. Emanuel, 1998: Dissipative heating and hurricane intensity. *Meteor. Atmos. Phys.*, **65**, 233–240, https://doi.org/10.1007/BF01030791.

Bryan, G. H., and J. M. Fritsch, 2002: A benchmark simulation for moist nonhydrostatic numerical model. *Mon. Wea. Rev.*, **130**, 2917–2928, https://doi.org/10.1175/1520-0493(2002)130<2917:ABSFMN>2.0.CO;2.

——, and R. Rotunno, 2009: The maximum intensity of tropical cyclones in axisymmetric numerical model simulations. *J. Atmos. Sci.*, **137**, 1770–1789, https://doi.org/10.1175/2008MWR2709.1.

Callen, H. B., 1985: *Thermodynamics and an Introduction to Thermostatistics*. Wiley, 493 pp.

Chavas, D. R., and K. A. Emanuel, 2014: Equilibrium tropical cyclone size in an idealized state of axisymmetric radiative–convective equilibrium. *J. Atmos. Sci.*, **71**, 1663–1680, https://doi.org/10.1175/JAS-D-13-0155.1.

——, and N. Lin, 2016: A model for the complete radial structure of the tropical cyclone wind field. Part II: Wind field variability. *J. Atmos. Sci.*, **73**, 3093–3113, https://doi.org/10.1175/JAS-D-15-0185.1.

——, and K. A. Reed, 2019: Dynamical aquaplanet experiments with uniform thermal forcing: System dynamics and implications for tropical cyclone genesis and size. *J. Atmos. Sci.*, **76**, 2257–2274, https://doi.org/10.1175/JAS-D-19-0001.1.

——, N. Lin, and K. A. Emanuel, 2015: A model for the complete radial structure of the tropical cyclone wind field. Part I: Comparison with observed structure. *J. Atmos. Sci.*, **72**, 3647–3662, https://doi.org/10.1175/JAS-D-15-0014.1.

——, ——, W. Dong, and Y. Lin, 2016: Observed tropical cyclone size revisited. *J. Climate*, **29**, 2923–2939, https://doi.org/10.1175/JCLI-D-15-0731.1.

——, K. A. Reed, and J. A. Knaff, 2017: Physical understanding of the tropical cyclone wind-pressure relationship. *Nat. Commun.*, **8**, 1360, https://doi.org/10.1038/s41467-017-01546-9.

Chen, J., and D. R. Chavas, 2020: The transient responses of an axisymmetric tropical cyclone to instantaneous surface roughening and drying. *J. Atmos. Sci.*, **77**, 2807–2834, https://doi.org/10.1175/JAS-D-19-0320.1.

Cronin, T. W., and D. R. Chavass, 2019: Dry and semidry tropical cyclones. *J. Atmos. Sci.*, **76**, 2193–2212, https://doi.org/10.1175/JAS-D-18-0357.1.

Dunnavan, G. M., and J. W. Diercks, 1980: An analysis of Super Typhoon Tip (October 1979). *Mon. Wea. Rev.*, **108**, 1915–1923, https://doi.org/10.1175/1520-0493(1980)108<1915:AAOSTT>2.0.CO;2.

Eliassen, A., and E. Kleinschmidt, 1957: Dynamic meteorology. *Geophysics II*, Springer, 1–154.

Emanuel, K. A., 1986: An air–sea interaction theory for tropical cyclones. Part I: Steady state maintenance. *J. Atmos. Sci.*, **43**, 585–605, https://doi.org/10.1175/1520-0469(1986)043<0585:AASITF>2.0.CO;2.

——, 1988: The maximum intensity of hurricanes. *J. Atmos. Sci.*, **45**, 1143–1155, https://doi.org/10.1175/1520-0469(1988)045<1143:TMIOH>2.0.CO;2.

——, 1989: The finite-amplitude nature of tropical cyclogenesis. *J. Atmos. Sci.*, **46**, 3431–3456, https://doi.org/10.1175/1520-0469(1989)046<3431:TFANOT>2.0.CO;2.

——, 1991: The theory of hurricanes. *Annu. Rev. Fluid Mech.*, **23**, 179–196, https://doi.org/10.1146/annurev.fl.23.010191.001143.

——, 1995: The behavior of a simple hurricane model using a convective scheme based on subcloud-layer entropy equilibrium. *J. Atmos. Sci.*, **52**, 3960–3968, https://doi.org/10.1175/1520-0469(1995)052<3960:TBOASH>2.0.CO;2.

——, 2004: Tropical cyclone energetics and structure. *Atmospheric Turbulence and Mesoscale Meteorology*, E. Fedorovich, R. Rotunno, and B. Stevens, Eds., Cambridge University Press, 165–192.

——, 2022: Tropical cyclone seeds, transition probabilities, and genesis. *J. Climate*, **35**, 3557–3566, https://doi.org/10.1175/JCLI-D-21-0922.1.

——, and R. Rotunno, 2011: Self-stratification of tropical cyclone outflow. Part I: Implications for storm structure. *J. Atmos. Sci.*, **68**, 2236–2249, https://doi.org/10.1175/JAS-D-10-05024.1.

Frank, W. M., 1977: The structure and energetics of the tropical cyclone. Part I: Storm structure. *Mon. Wea. Rev.*, **105**, 1119–1135, https://doi.org/10.1175/1520-0493(1977)105<1119:TSAEOT>2.0.CO;2.

Hakim, G. J., 2011: The mean state of axisymmetric hurricanes in statistical equilibrium. *J. Atmos. Sci.*, **68**, 1364–1376, https://doi.org/10.1175/2010JAS3644.1.

Kepert, J., and Y. Wang, 2001: The dynamics of boundary layer jets within the tropical cyclone core. Part II: Nonlinear enhancement. *J. Atmos. Sci.*, **58**, 2485–2501, https://doi.org/10.1175/1520-0469(2001)058<2485:TDOBLJ>2.0.CO;2.

Khairoutdinov, M., and K. Emanuel, 2013: Rotating radiative-convective equilibrium simulated by a cloud-resolving model. *J. Adv. Model. Earth Syst.*, **5**, 816–825, https://doi.org/10.1002/2013MS000253.

Lu, K.-Y., and D. Chavas, 2022: Tropical cyclone size is strongly limited by the Rhines scale: Experiments with a barotropic model. *J. Atmos. Sci.*, **79**, 2109–2124, https://doi.org/10.1175/JAS-D-21-0224.1.

Maclay, K. S., M. DeMaria, and T. H. Vonder Haar, 2008: Tropical cyclone inner-core kinetic energy evolution. *Mon. Wea. Rev.*, **136**, 4882–4898, https://doi.org/10.1175/2008MWR2268.1.

Martinez, J., C. C. Nam, and M. M. Bell, 2020: On the contributions of incipient vortex circulation and environmental moisture to tropical cyclone expansion. *J. Geophys. Res. Atmos.*, **125**, e2020JD033324, https://doi.org/10.1029/2020JD033324.

Merrill, R. T., 1984: A comparison of large and small tropical cyclones. *Mon. Wea. Rev.*, **112**, 1408–1418, https://doi.org/10.1175/1520-0493(1984)112<1408:ACOLAS>2.0.CO;2.

Morrison, H., J. A. Curry, and V. I. Khvorostyanov, 2005: A new double-moment microphysics scheme for application in cloud and climate models. Part I: Description. *J. Atmos. Sci.*, **62**, 1665–1677, https://doi.org/10.1175/JAS3446.1.

Pauluis, O. M., 2011: Water vapor and mechanical work: A comparison of Carnot and steam cycles. *J. Atmos. Sci.*, **68**, 91–102, https://doi.org/10.1175/2010JAS3530.1.

——, and I. M. Held, 2002: Entropy budget of an atmosphere in radiative–convective equilibrium. Part I: Maximum work and frictional dissipation. *J. Atmos. Sci.*, **59**, 125–139, https://doi.org/10.1175/1520-0469(2002)059<0125:EBOAAI>2.0.CO;2.

——, and F. Zhang, 2017: Reconstruction of thermodynamic cycles in a high-resolution simulation of a hurricane. *J. Atmos. Sci.*, **74**, 3367–3381, https://doi.org/10.1175/JAS-D-16-0353.1.

——, V. Balaji, and I. M. Held, 2000: Frictional dissipation in a precipitating atmosphere. *J. Atmos. Sci.*, **57**, 989–994, https://doi.org/10.1175/1520-0469(2000)057<0989:FDIAPA>2.0.CO;2.

Romps, D. M., 2008: The dry-entropy budget of a moist atmosphere. *J. Atmos. Sci.*, **65**, 3779–3799, https://doi.org/10.1175/2008JAS2679.1.

Rotunno, R., and K. A. Emanuel, 1987: An air–sea interaction theory for tropical cyclones. Part II: Evolutionary study using a nonhydrostatic axisymmetric numerical model. *J. Atmos. Sci.*, **44**, 542–561, https://doi.org/10.1175/1520-0469(1987)044<0542:AAITFT>2.0.CO;2.

——, and G. H. Bryan, 2012: Effects of parameterized diffusion on simulated hurricanes. *J. Atmos. Sci.*, **69**, 2284–2299, https://doi.org/10.1175/JAS-D-11-0204.1.

Rousseau-Rizzi, R., and K. A. Emanuel, 2019: An evaluation of hurricane superintensity in axisymmetric numerical models. *J. Atmos. Sci.*, **76**, 1697–1708, https://doi.org/10.1175/JAS-D-18-0238.1.

——, R. Rotunno, and G. Bryan, 2021: A thermodynamic perspective on steady-state tropical cyclones. *J. Atmos. Sci.*, **78**, 583–593, https://doi.org/10.1175/JAS-D-20-0140.1.

Tang, B., and K. Emanuel, 2010: Midlevel ventilation's constraint on tropical cyclone intensity. *J. Atmos. Sci.*, **67**, 1817–1830, https://doi.org/10.1175/2010JAS3318.1.

——, and ——, 2012: A ventilation index for tropical cyclones. *Bull. Amer. Meteor. Soc.*, **93**, 1901–1912, https://doi.org/10.1175/BAMS-D-11-00165.1.

Tao, D., M. Bell, R. Rotunno, and P. J. Van Leeuwen, 2020: Why do the maximum intensities in modeled tropical cyclones vary under the same environmental conditions? *Geophys. Res. Lett.*, **47**, e2019GL085980, https://doi.org/10.1029/2019GL085980.

Wang, D., and Y. Lin, 2021: Potential role of irreversible moist processes in modulating tropical cyclone surface wind structure. *J. Atmos. Sci.*, **78**, 709–725, https://doi.org/10.1175/JAS-D-20-0192.1.

Zhou, W., I. M. Held, and S. T. Garner, 2014: Parameter study of tropical cyclones in rotating radiative–convective equilibrium with column physics and resolution of a 25-km GCM. *J. Atmos. Sci.*, **71**, 1058–1069, https://doi.org/10.1175/JAS-D-13-0190.1.

CORRIGENDUM

DANYANG WANG,[a,b] YANLUAN LIN,[a] AND DANIEL R. CHAVAS[b]

[a] *Ministry of Education Key Laboratory for Earth System Modeling, Department of Earth System Science, Tsinghua University, Beijing, China*
[b] *Purdue University, West Lafayette, Indiana*

(Manuscript received 19 March 2023, accepted 24 April 2023)

This corrigendum is to report a known error in Wang et al. (2022) entitled "Tropical Cyclone Potential Size" (TC PS). The error is that the reported w_{cool} diagnosed from CM1 simulations (section 3) is about half of the true value, as a result of a mistake in the code of its calculation. Thus, the first sentence on p. 3018 should be corrected as "The value of w_{cool} is approximately 0.0027 m s^{-1} when SST = 300 K; it increases to ~0.006 m s^{-1} when SST = 280 K."

The incorrect value of w_{cool} was put into the TC PS model to compare with CM1 results (Figs. 10 and 11 of Wang et al. 2022). Thus, we need to evaluate the error induced in Figs. 10 and 11. The overall nice match of both r_a (outer radius of vanishing winds) and p_m (near surface pressure at radius of maximum wind r_m) in Figs. 10 and 11 suggests that the TC PS model is not strongly sensitive to w_{cool}; thus, the error is estimated to be small and does not affect the conclusion(s) drawn from Figs. 10 and 11. Because the first author is not able to access the original model output, we do not provide direct updates of Figs. 10 and 11 here. Instead, we demonstrate below the general weak sensitivity of the TC PS model to w_{cool} by a sensitivity test in which the range of w_{cool} tested is wider than the error itself.

In the TC PS model, w_{cool} is put into Chavas et al. (2015, hereafter C15) wind model for the p_m and r_m (for calculation of M_m, the absolute angular momentum at r_m) predicted by C15 model. First, we show C15 model predicted p_m is not very sensitive to w_{cool} (Fig. 1). The p_m only changes by ~5 hPa with a 6-times difference of w_{cool} (0.001 35 to 0.0081 m s^{-1}). Indeed, TC PS predictions are weakly sensitive to w_{cool}, as shown by Figs. 2 and 3. The effect of w_{cool} in affecting TC PS prediction by modulating M_m is small as M_m is by itself only a small portion (~10%) of M_a (absolute angular momentum at r_a), which is responsible for the "outflow work" in TC PS model.

Given that the TC PS model is only weakly sensitive to w_{cool}, the nice match of the TC PS prediction and CM1 results in Figs. 10 and 11 of Wang et al. (2022) should still hold with correct w_{cool}.

Another relevant calculation is the corresponding r_a (section 3) estimated from Emanuel (2004, hereafter E04) model by fitting to simulated r_4. The incorrect (too small) w_{cool} would increase r_a by doubling the $C_d V_{gm}/w_{cool}$ factor in E04 model [Eq. (21) of Wang et al. 2022]. Coincidentally, though, doubling this factor appears reasonable in the tail of the wind profile because we included a surface gustiness of 5 m s^{-1} in CM1 [Eq. (30) of Wang et al. 2022], which would effectively increase surface drag. Thus, the original estimate of r_a in Wang et al. (2022) is still considered reasonable.

REFERENCES

Chavas, D. R., N. Lin, and K. A. Emanuel, 2015: A model for the complete radial structure of the tropical cyclone wind field. Part I: Comparison with observed structure. *J. Atmos. Sci.*, **72**, 3647–3662, https://doi.org/10.1175/JAS-D-15-0014.1.

Emanuel, K. A., 2004: Tropical cyclone energetics and structure. *Atmospheric Turbulence and Mesoscale Meteorology*, E. Fedorovich, R. Rotunno, and B. Stevens, Eds., Cambridge University Press, 165–192.

Wang, D., Y. Lin, and D. Chavas, 2022: Tropical cyclone potential size. *J. Atmos. Sci.*, **79**, 3001–3025, https://doi.org/10.1175/JAS-D-21-0325.1.

Corresponding author: Yanluan Lin, yanluan@tsinghua.edu.cn

DOI: 10.1175/JAS-D-23-0042.1

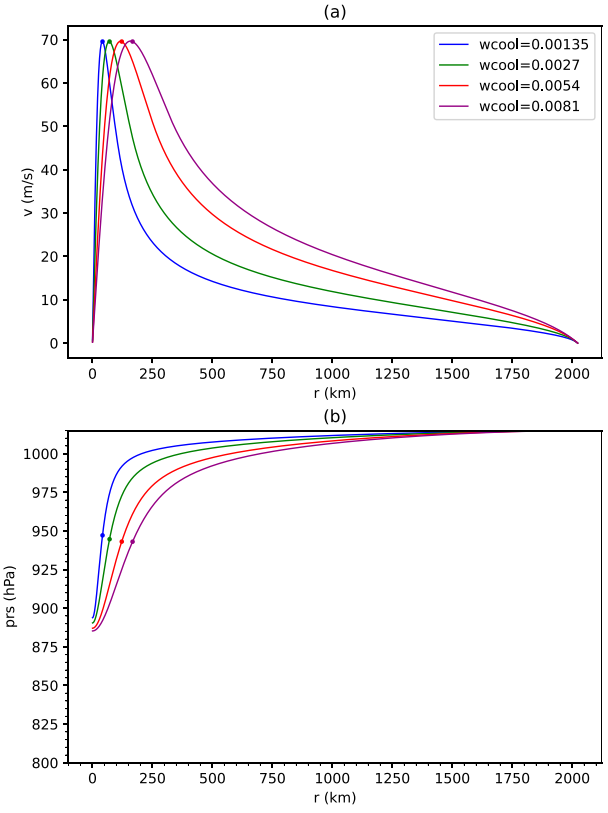

FIG. 1. This figure helps explain why quantitatively small changes of Figs. 10 and 11 in Wang et al. (2022) are expected if correct w_{cool} were used. (a) C15 model predicted wind profile (m s^{-1}) with different w_{cool} (m s^{-1}; see legends); (b) the corresponding surface pressure profile following gradient wind balance. The dots mark r_m and the corresponding tangential velocity in (a) and p_m in (b). Environment settings other than w_{cool} are the same as Fig. 4 of Wang et al. (2022). In the calculation of surface pressure by gradient wind balance, air density is simply approximated by ideal gas law ignoring water vapor.

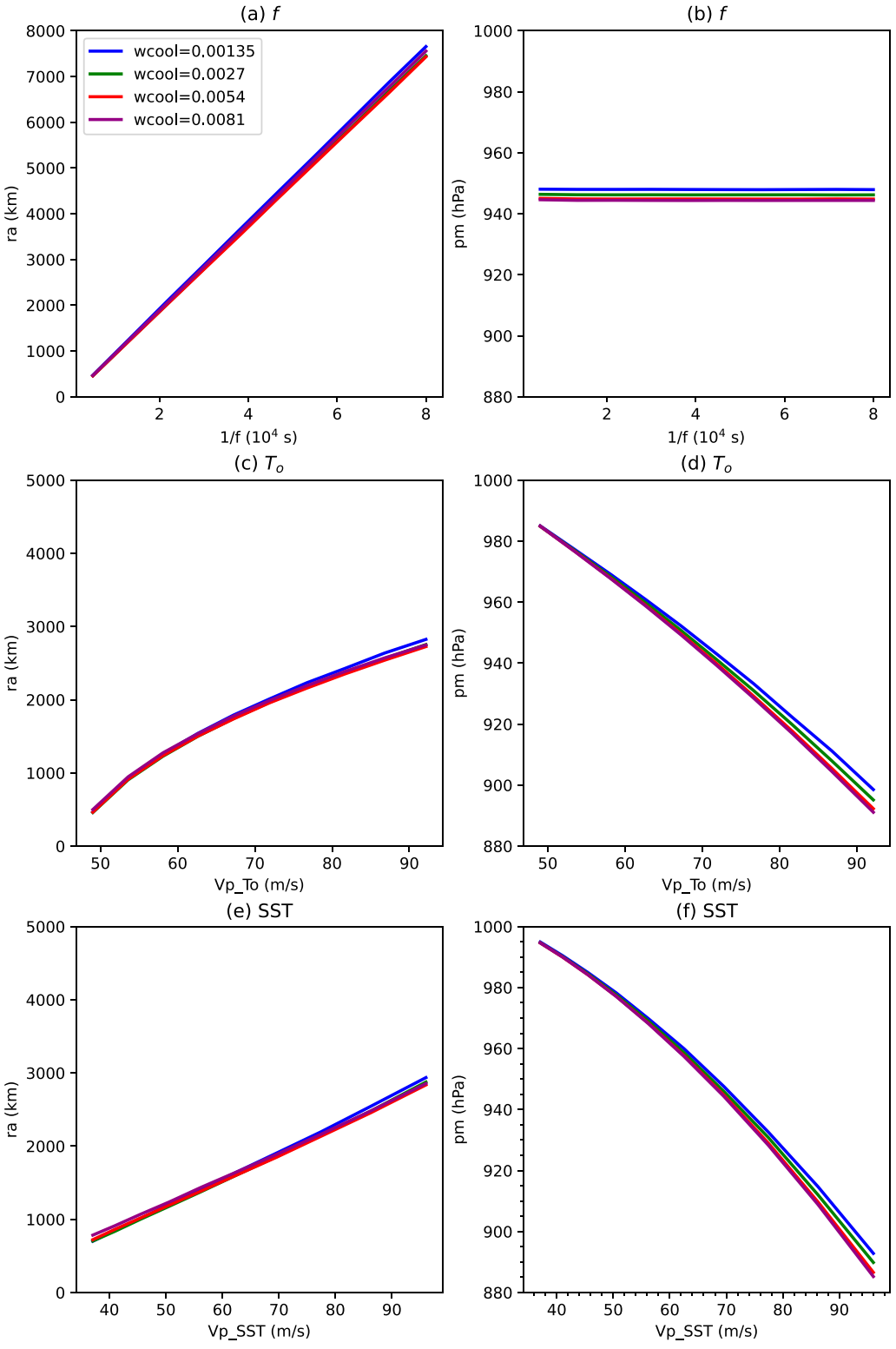

FIG. 2. This figure demonstrates why quantitatively small changes of Fig. 10 in Wang et al. (2022) are expected if correct w_{cool} were used. TC PS model prediction of (a),(c),(e) r_a (km) and (b),(d),(f) p_m (hPa) for a range of values of w_{cool} (m s^{-1}; see legends) and with variable (top) Coriolis parameter f, (middle) tropopause (outflow) temperature, and (bottom) sea surface temperature. Environment settings other than w_{cool} are the same as Fig. 5 of Wang et al. (2022), with the exception that $\eta = 0.4$, $r_o = 1.25r_a$ is used following section 3 of Wang et al. (2022), and outflow temperature spans from 160 to 240 K in (c) and (d). This figure follows Fig. 5 of Wang et al. (2022).

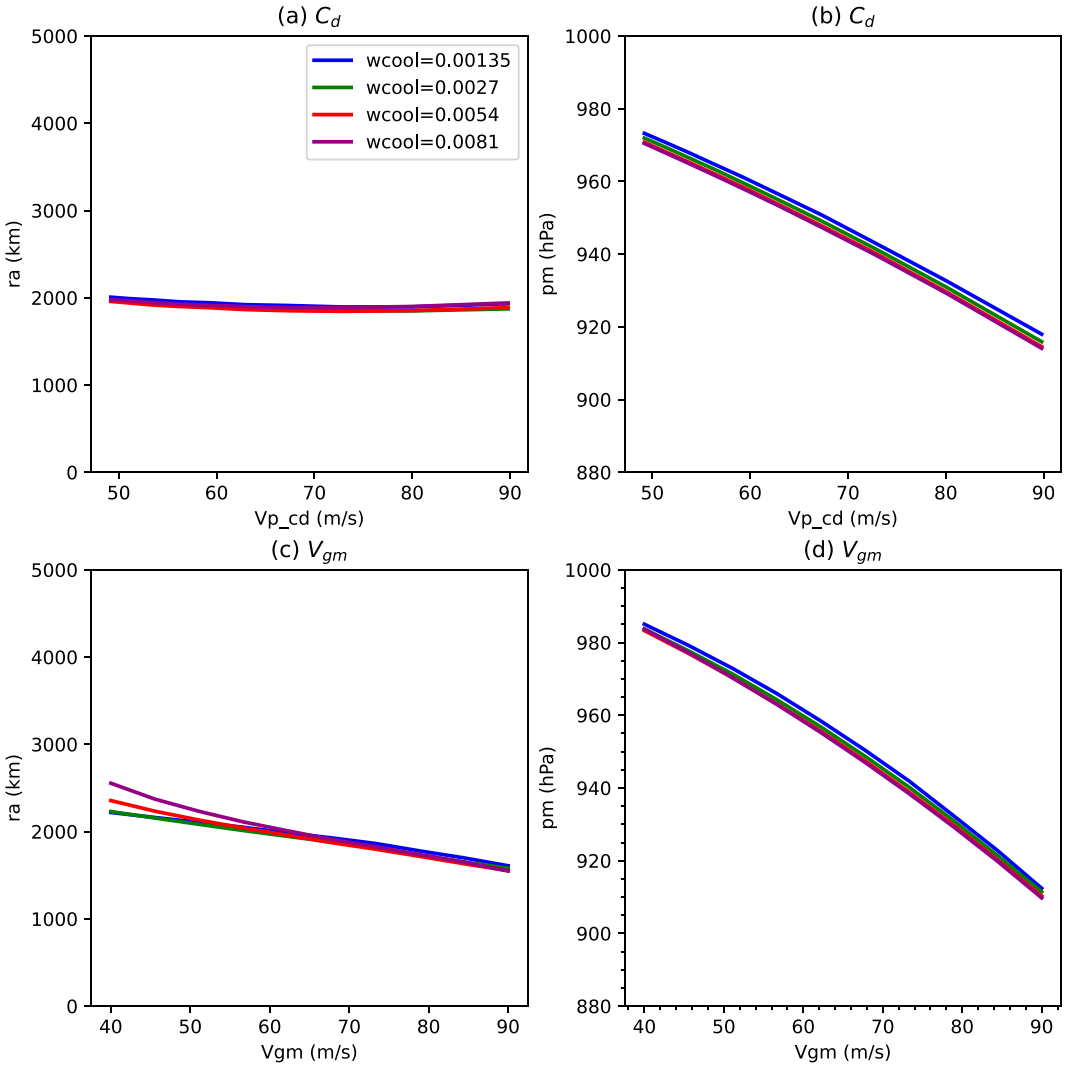

FIG. 3. This figure demonstrates why quantitatively small changes of Fig. 11 in Wang et al. (2022) are expected if correct w_{cool} were used. As in Fig. 2, but with variable (top) surface exchange coefficient for momentum C_d and (bottom) maximum gradient wind V_{gm}. Environment settings other than w_{cool} are the same as Fig. 6 of Wang et al. (2022), with the exception of $\eta = 0.4$, $r_o = 1.25r_a$. This figure follows Fig. 6 of Wang et al. (2022). The test with a varied exchange coefficient for enthalpy C_k is not included because it does not modulate V_p in our simulation setup and it is not varied in Figs. 11c and 11d of Wang et al. (2022).